UNIVERSITY OF CALIFORNIA
Santa Barbara

Emergent States and Magnetism in Perovskite Titanate Heterostructures

A Dissertation submitted in partial satisfaction
of the requirements for the degree of

Doctor of Philosophy

in

Materials

by

Clayton Adam Chase Jackson

Committee in Charge:

Professor Susanne Stemmer, Chair

Professor S. James Allen

Professor Chris Palmstrøm

Professor James S. Speck

September 2014

The Dissertation of
Clayton Adam Chase Jackson is approved:

Professor S. James Allen

Professor Chris Palmstrøm

Professor James S. Speck

Professor Susanne Stemmer, Committee Chairperson

September 2014

Emergent States and Magnetism in Perovskite Titanate Heterostructures

by

Clayton Adam Chase Jackson

To my Mom and Dad, and my brothers Phil,

Nathan, and Aaron

How precious are your thoughts to me, o God! How vast is the sum of them! If I should count them, they would be more in number than the sand; when I awake, I am still with you.

Acknowledgements

I first and foremost want to express my gratitude to my advisor, Susanne Stemmer, who has given me opportunity, guidance, and instruction over the past four years. She has always made herself available to her students, for which I am thankful. I would also like to acknowledge my appreciation for my committee; Jim Speck, Chris Palmtrøm and Jim Allen. Jim Allen in particular has taken a strong interest in my work and I have had the great fortune of working with him closely on many projects. The depth of his experimental insight and intelligence is matched only by his humble nature; It has been a joy to work under his guidance.

In addition to my committee, I must express my gratitude for the group I have had the privilege to work with these past four years. We have shared in frustrations and triumphs and if it were not for one another, I cannot say with certitude I would still be finishing this race. Pouya, Tyler, Adam, Jack, Jinwoo, Gift, Santosh, Evgeny, Chris, Patrick, Brandon; Thank you. In particular, Pouya, Tyler, Adam, Santosh and Chris, It has been a huge blessing to have worked so closely with you all in the MBE lab.

One of the most fantastic aspects of graduate school in Materials at UCSB is the depth of resources available to the students through shared facilities, certainly not possible without the diligence of the staff members. I must extend my gratitude to all the members of the nanofabrication facility (especially Don Freeborn), Joe and Amanda for managing the TEMPO lab in the MRL, Youli Li for his help in the XRD lab, and

most especially, John English for putting up with me and for being infinitely helpful and patient in the MBE lab.

Curriculum Vitæ

Clayton Adam Chase Jackson

Education

- **Ph.D. Materials Science, University of California, Santa Barbara** ***2010-2014***
- **B.S. (Honors) Physics, GPA 3.87, University of Texas at Austin** ***2006-2010***

Awards

- **National Science Foundation Graduate Research Fellowship (2012-2015)**
- Materials Research Laboratory / DOW Travel Fellowship, University of California, Santa Barbara (2012-2014)
- UC Santa Barbara Barpal Fellowship (2011-2013)
- Distinguished Graduating Senior Award (2010)
- Distinguished College Scholar (2010)
- Dr. Arnold Romberg Endowed Scholarship in Physics (2009-2010)
- Melvin J. Rieger Scholarship (2009)
- Undergraduate Research Fellowship (2008)

Professional Appointments

- Graduate Student Researcher, University of California, Santa Barbara *2010-2014*
- Grading Assistant, University of California, Santa Barbara *Fall 2013*
- Teaching Assistant, University of California, Santa Barbara *Winter 2012*
- Undergraduate Research Assistant, University of Texas at Austin *2008-2010*

Publications

- **C. A. Jackson**, J. Y. Zhang, C. R. Freeze, and S. Stemmer. Quantum critical behavior in confined $SrTiO_3$ quantum wells embedded in antiferromagnetic $SmTiO_3$. *Nat. Commun.* 5, 4258 (2014) [doi]
- M. Boucherit, O. F. Shoron, **C. A. Jackson**, T. A. Cain, M. L. C. Buffon, C. Polshinsku, S. Stemmer and S. Rajan. Modulation of over 10^{14} cm^{-2} electrons in $SrTiO_3$/$GdTiO_3$ heterostructures. *Appl. Phys. Lett.* **104**, 182904 (2014) [doi]
- J. Y. Zhang, **C. A. Jackson**, R. Chen, S. Raghavan, P. Moetakef, L. Balents, and S. Stemmer. Correlation between metal-insulator transitions and structural distortions in high-electron-density $SrTiO_3$ quantum wells. *Phys. Rev. B* **89**, 075140 (2014) [doi]
- **C. A. Jackson** and S. Stemmer. Interface-induced magnetism in perovskite quantum wells. *Phys. Rev. B* **88**, 180403(R) (2013) [doi]
- J. Y. Zhang*, **C. A. Jackson***, S. Raghavan, J. Hwang, and S. Stemmer. Magnetism and local structure in low-dimensional Mott insulating $GdTiO_3$. *Phys. Rev. B* **88**, 121104(R) *equal contributors (2013) [doi]

- M. Boucherit, O. F. Shoron, T. A. Cain, **C. A. Jackson**, S. Stemmer, and S. Rajan. Extreme charge density $SrTiO_3/GdTiO_3$ heterostructure field effect transistors. *Appl. Phys. Lett.* **102**, 242909 (2013) [doi]

- P. Moetakef, **C. A. Jackson**, J. Hwang, L. Balents, S. J. Allen, and S. Stemmer. Toward an artificial Mott insulator: Correlations in confined, high-density electron liquids in $SrTiO_3$. *Phys. Rev. B* **86**, 201102(R) (2012) [doi]

- T. A. Cain, P. Moetakef, **C. A. Jackson**, and S. Stemmer. Modulation doping to control the high-density electron gas at a polar/non-polar oxide interface. *Appl. Phys. Lett.* **101**, 111604 (2012) [doi]

- **C. A. Jackson**, P. Moetakef, S. J. Allen, and S. Stemmer. Capacitance-voltage analysis of high-carrier-density $SrTiO_3/GdTiO_3$ heterostructures. *Appl. Phys. Lett.* **100**, 232106 (2012) [doi]

Abstract

Emergent States and Magnetism in Perovskite Titanate Heterostructures

Clayton Adam Chase Jackson

Complex oxides show a wide array of phenomena, including magnetic states, ferroelectricity, and superconductivity. Furthermore, the advent of atomic scale engineering of the oxides using molecular beam epitaxy (MBE) has facilitated the discovery of novel phenomena in thin films and heterostructures not seen in bulk. Complex oxide perovskite titanate heterostructures composed of both Mott and band insulators can be fabricated readily and exhibit unique properties, including interfacial two-dimensional electron gases (2DEGs), superconductivity, and magnetic ordering.

The objective of this Dissertation is to study the relationships between emergent phenomena and heterostructure design using advanced MBE growth techniques and characterization tools, with the intent of developing controllable states of matter. The impact of strain and octahedral connectivity in epitaxially mismatched heterostructures on magnetism and electrical transport is addressed, as well as proximity effects and the influence of magnetically ordered layers on neighboring low-dimensional itinerant systems.

The Dissertation begins with a motivational overview of materials and associated phenomena, describing the unique emergent properties associated with thin films. This

is followed by a description of the organization of the remainder of the text. The methods implemented, including MBE and electrical transport characterization, are then discussed. Structure-magnetism and structure-transport correlations are demonstrated, as well as *tunable* emergent ferromagnetism in $GdTiO_3/SrTiO_3$ heterostructures and quantum critical behavior in $SmTiO_3/SrTiO_3$ heterostructures. Recent progress on devices based on $GdTiO_3/SrTiO_3$ are discussed. The dissertation closes with a brief summary and discussion of future works.

Contents

List of Tables

List of Figures

Chapter 1

Introduction

1.1 Introduction

Complex oxide titanates show a wide array of interesting phenomena, including magnetic states, ferroelectricity, multiferrocity and superconductivity. While these oxides show unique bulk properties, these studies are often limited by their inherent complexity (for instance, chemical doping, a common control parameter in bulk studies, convolutes the resulting physics by introducing *both* disorder and charge) and lack of control of dimensionality [6, 7]. To allow for atomic layer precision, a growth synthesis technique [8, 5] has been developed for complex oxide thin films and thin film heterostructures. Atomic scale engineering with molecular beam epitaxy (MBE) has facilitated the discovery of entirely new features in thin films and heterostructures, as well as provide a new avenue of device engineering based on oxide electronics. Complex oxide heterostructures composed of Mott and band insulators exhibit unique features not seen in the bulk and play host to a variety of emergent phenomena including two-dimensional electron gases (2DEGs) and highly conductive interfaces, superconductivity, and magnetic ordering [9, 10, 11, 12] as well as coexistence of ferromagnetism and superconductivity [11].

The application of MBE to oxides has enabled the realization of unique phenomena including quantum confinement, electrostatic doping, and unique spin, charge and orbital ordering. Much work has focused on emergent properties in complex oxide het-

erostructures [13, 14, 15, 16], and the field shows great promise for future discovery. However, many questions remain unanswered, as this field is still in its infancy. It is well understood that orbital order (concomitantly, the structural Ti-O array) plays a pivotal role in the bulk magnetic properties of the titanates [17], but the impact of strain and octahedral connectivity in epitaxially mismatched heterostructures on magnetism is not fully understood. Compelling evidence for emergent magnetic states has been observed in Mott/band heterostructures [11], but the influence of proximity effects and exchange coupling has yet to be completely resolved. Furthermore, the influence of magnetically ordered layers on neighboring low-dimensional itinerant systems could promote novel states, such as quantum criticality and superconductivity [18, 19, 20, 21].

This dissertation is concerned with understanding the nature of these emergent phenomena in Mott/band insulator heterostructures, their relation to one another, and developing methods to *control* these unique properties by *design*. More specifically, we seek to understand the role of thin film design, magnetism and proximity effects in heterostructures. In the remainder of this chapter, we will discuss the specific systems of interest, and recent progress in this field.

Our focus is on the class of materials that adopt a crystal structure characterized by the chemical formula $\mathbf{ABO}_3$ called *perovskites*. This is a large family of ceramic materials whose structure is based on perovskite $CaTiO_3$, named for the mineralogist Aleksevich von Perovski [22].

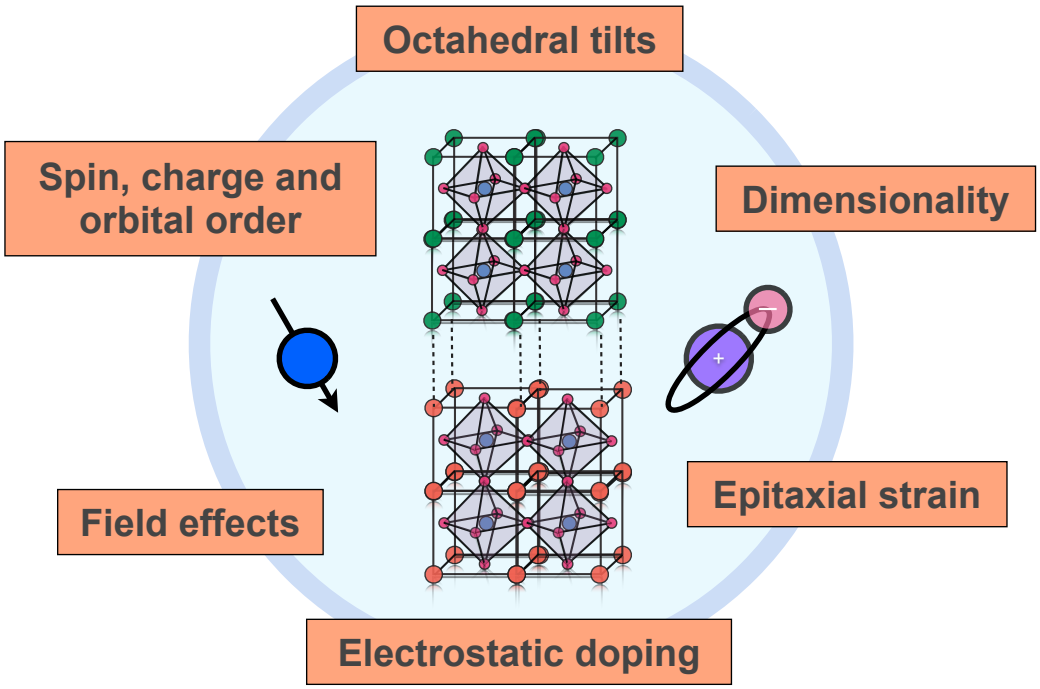

Figure 1.1: Illustration of different features exhibited by thin film heterostructures that can be utilized and tuned to produce and control emergent phenomena.

The structure, illustrated in Figure 1.2, is idealized as cubic, but will readily adopt tetragonal or orthorhombic distortions, accommodated by tilting of the oxygen octahedra. The propensity for this structure to allow for a wide variety of A and B cations with subtle variations in geometric distortion gives rise to a wide array of phenomena, including magnetic insulating states [1, 17], ferroelectricity [23, 24] and superconductivity [25].

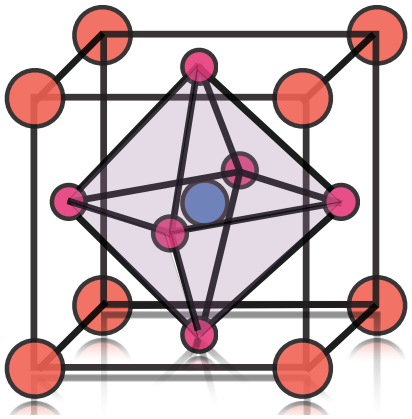

Figure 1.2: Illustration of the perovskite crystal structure, where the central atom is the B-site, surrounded by an octahedra formed by face-centered oxygen atoms. The corners of the cube are the A-site.

Among the perovskites, this work is most interested in heterostructures composed of rare-earth titanates. These are Mott materials that adopt the aforementioned perovskite structure, distorted into an orthorhombic $GdFeO_3$ structure (space group *Pbnm*). Unlike traditional materials, which can be described in the effective mass approximation, Mott materials require accounting for the Coulombic interaction of electrons to explain their unique properties. A physical framework proposed by Mott and Hubbard [26, 27, 28] that has been successful in explaining some phenomena exhibited by Mott materials is an augmented tight-binding approximation. In addition to the normal tight-binding Hamiltonian, an additional term arises from an energy penalty associated with conduction (the Hubbard U), a result of Coulombic repulsion between electrons. This can be described by considering a band composed of s-orbitals, each harboring a sin-

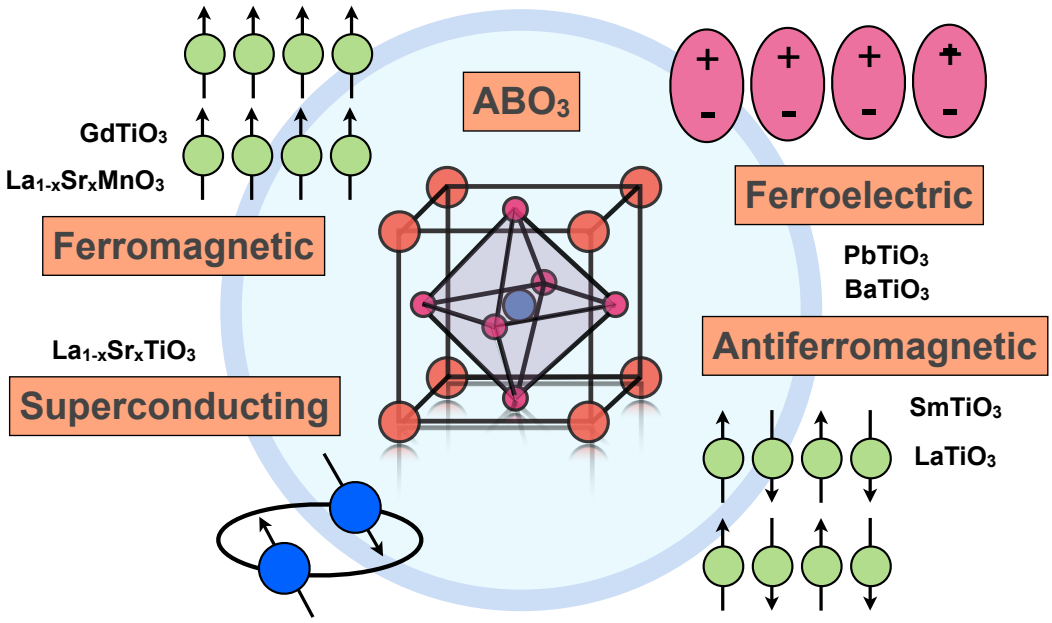

Figure 1.3: Overview of phenomena associated with materials that adopt a perovskite crystal structure.

gle electron. Each orbital can accommodate two electrons with opposite spin, a direct consequence of Pauli exclusion. However, double occupancy arising from hopping conduction is suppressed by a strong Coulombic interaction between electrons that are forced into relatively close proximity. Thus, double occupancy results in the splitting into upper and lower Hubbard bands and an insulating state.

Phenomena related to electron correlation include superconductivity and magnetic ordering [9, 10, 29, 11] as well as spin and orbital ordering leading to mass enhance-

ment and colossal magnetoresistance [30, 31, 32]. Experimental insights into the physics of heterostructures containing Mott materials contribute to a deeper understanding of these phenomena and their potential applications. Much current research is focused on understanding any discrepancies between an ideal Mott material and real material systems, understanding how the material arrives at an insulating state and why this phenomenon is exhibited in some materials but not others [33, 34, 35, 36, 12, 1].

The rare-earth titanates are known to adopt different magnetic insulating states resulting from distortions and tilts of the moment associated with the Ti-O octahedra in the orthorhombic $GdFeO_3$ structure. These distortions will result in different favored super-exchange interactions within the Ti-O complex and any moment associated with the rare-earth [17]. Two types of orbital ordering have been reported, ferro-orbital and antiferro-orbital. Both are compatible with *Pbnm* symmetry [37, 38, 39, 40, 41, 42]. Ferro-orbital ordering is associated with antiferromagnetism, typical of smaller $GdFeO_3$-type distortions (A = La.....Sm in the chemical formula $ATiO_3$), while larger distortion lends itself to antiferro-orbital ordering and is associated with ferromagnetism (A = Gd.....Y).

The two Mott insulating rare-earth titanates of interest to this work are $GdTiO_3$ and $SmTiO_3$. Both have a d^1 electron configuration. $SmTiO_3$ has a slightly less distorted orthorhombic crystal structure than $GdTiO_3$ [43]. $GdTiO_3$ is ferrimagnetic while

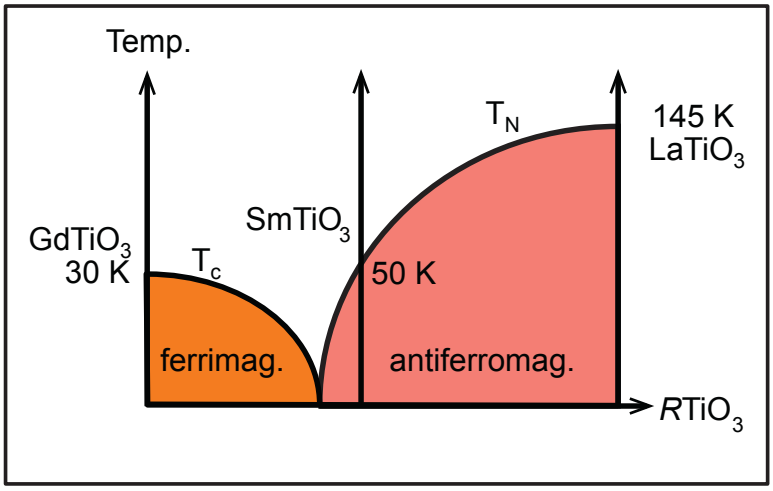

Figure 1.4: Phase diagram illustrating the relationship between A-site cation and magnetic order for some of the rare-earth titanates (Gd to La) [1].

$SmTiO_3$ is antiferromagnetic [1]. The magnetism is a result of different orbital ordering; antiferro-orbital in $GdTiO_3$ and ferro-orbital in $SmTiO_3$ [39, 44, 37].

In this work, these materials are interfaced with the band insulator $SrTiO_3$. This interface readily forms a high density 2DEG, a result of polar discontinuity [15]. Charge transfer results in a highly conductive interface with a carrier concentration of approximately 3×10^{14} cm^{-2}, 1/2 an electron per 2D interfacial unit cell. This has been observed in many material systems, including $LaAlO_3/SrTiO_3$ [9, 29, 11], $LaTiO_3/SrTiO_3$ [10], $GdTiO_3/SrTiO_3$ and $SmTiO_3/SrTiO_3$ [45, 2]. For heterostructures consisting of

the rare-earth titanates, band offsets favor charge in the $SrTiO_3$, tightly bound to the interface [46].

1.2 Organization

Our objective is to study the relationships between emergent phenomena and heterostructures using advanced growth and characterization techniques, with the intent of developing controllable states of matter by design. The systems of choice are Mott/band insulator heterostructures composed of $SmTiO_3$, $GdTiO_3$ and $SrTiO_3$. We have shown that structures of this kind show a variety of interesting features, many of which are not fully understood. In this chapter, a motivational overview of the present status of research and open questions was given. To answer these questions concerning emergent phenomena in Mott/Band insulator thin film heterostructures, we must be able to efficiently design, produce and characterize them. Thus, this dissertation is broken down into the following objectives:

- Establish methods for growth and analysis
- Control of magnetic and transport properties through *structural* design
- Illucidate proximity effects in Mott/band insulator heterostructures
- Observation of novel emergent phenomena in oxide heterostructures

- Device design and engineering for electronic applications
- Discussion of future works

To assist the reader, Chapter 2 focuses on experimental methods used to grow and characterize structures discussed throughout the text. Next, Chapter 3 describes structure-magnetism and structure-transport correlations. Chapter 4 demonstrates the advent of a metallic ferromagnetic state in $SrTiO_3$ embedded in $GdTiO_3$, which can be controlled by heterostructure design. In Chapter 5, similar structures are discussed, in which the $GdTiO_3$ is replaced by antiferromagnetic $SmTiO_3$, resulting in the advent of a quantum critical state of matter, in which the control parameter is quantum well width. Chapter 6 discusses utilizing the conductive Mott-band insulator interface for device applications. Finally, Chapter 7 provides a summary and explores possible future works.

Chapter 2

Methods

2.1 Introduction

In order to address the open questions established in Chapter 1, namely, the relationships between structure, transport and magnetism in thin film heterostructures, we must be able to accurately produce and characterize them. We wish to understand the role of octahedral connectivity and proximity effects at atomically abrupt interfaces that lead to emergent phenomena, requiring atomic layer precision in crystal growth. These effects are subtle, thus requiring very high purity samples. Furthermore, we require characterization techniques that can provide insight into a number of different phenomena, including both electronic and magnetic structure.

In this chapter, we survey the primary growth and characterization tools employed to meet these requirements. For growth, we rely exclusively on a hybrid MBE technique, in which a metal-organic precursor element acts to supply oxygen and titanium. The primary characterization tool used is transport; It will be shown that transport can provide information concerning lattice structure (disorder), magnetism and evidence for emergent states.

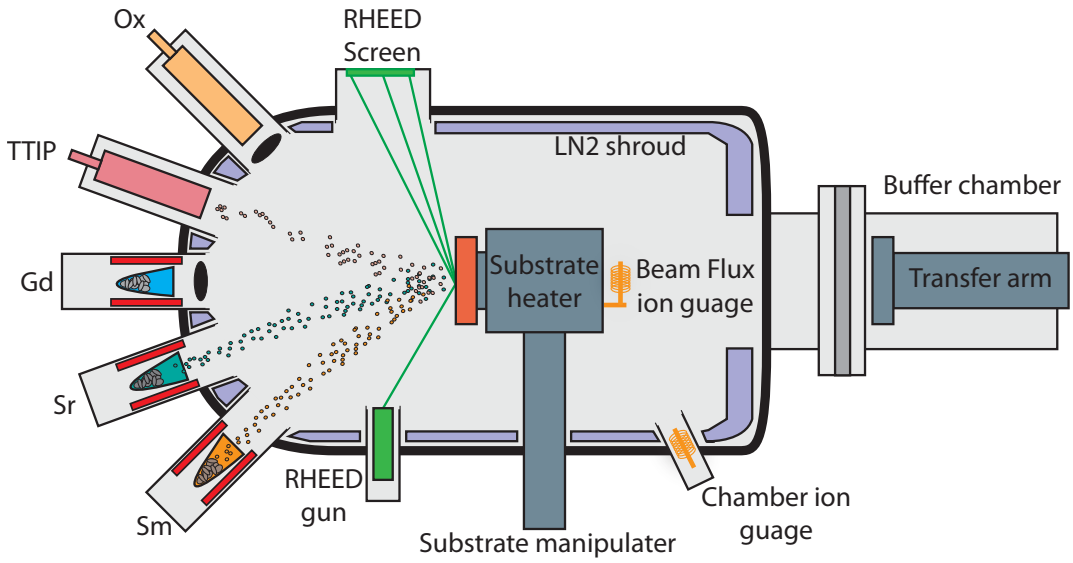

Figure 2.1: A schematic illustrating the primary features of a molecular beam epitaxy reactor.

2.2 Molecular beam epitaxy

Fundamentals of molecular beam epitaxy

MBE is a thin film growth technique in which source material is vaporized, typically in a heated effusion cell, producing a molecular beam that travels through ultra high vacuum (UHV) and impinges upon a heated substrate. Other methods to supply a molecular beam include electron-beam and gas sources. If the conditions are correct, the film grows as a crystal. Low growth rates, on the order $\sim$ 1 - 3 μm/hr for III-V semiconductors [47, 48], $\sim$ 180 nm/hr in the case of $SrTiO_3$ [49] and as low as $\sim$ 20 nm/hr for the rare earth titanates allow for atomic layer precision. The ultra high

vacuum results in extremely low unintentional doping. Furthermore, MBE offers the advantage of *in situ* characterization methods such as reflection high energy electron diffraction (RHEED), allowing for precise control of complex structures.

In the case of solid source MBE, the flux and energy distribution of the impinging species on the substrate are dictated by the effusion cell temperature T_i. If the atoms reevaporate from the substrate surface, they cary with them an energy proportional to their evaporating temperature $\propto T_e$. If they stay and reach thermal equilibrium with the substrate, they will have an energy proportional to the substrate temperature $\propto T_s$. The thermal accommodation coefficient is then $\alpha = (T_i\text{-}T_e)/(T_i\text{-}T_s)$. The sticking coefficient s is defined as the ratio of adhering atoms to the total number of arriving atoms at the substrate and is given by $s = N_{adh}/N_{tot}$. The pressure from a solid source is related to the materials enthalpy of evaporation ΔH and the cell temperature T by [50, 51]

$$p \propto e^{\frac{\Delta H}{k_B T}}. \tag{2.1}$$

The ideal flux from a given source (typically an effusion cell) can be expressed as

$$\phi = p\sqrt{\frac{N_A}{2\pi M k_B T}} \quad (m^{-2}s^{-1}), \tag{2.2}$$

where N_A is Avogadro's number, M the molecular weight of the impinging species, p the equilibrium pressure from the source and k_B Boltzmann's constant. This is the Hertz-Knudson equation [50].

The need for UHV

It is imperative to consider the minimum background pressure permissible to ensure that the molecular beam reaches the substrate. The two main considerations are the mean free path of the molecular species from the source, and the incorporation of impurities from residual background pressure.

The highest value of the background pressure allowable in the chamber is one such that the mean free path of the beam exceeds the distance from the cell to the substrate, and is given by the allowable partial pressure of residual gas

$$p_g = k_b T \frac{1/L_b - \sqrt{2}\pi n_b d_b^2}{\pi/4(d_b + d_g)^2}, \tag{2.3}$$

where n_b and d_b are the concentration and diameter of the constituents of the molecular beam and d_g the concentration of any residual gas in the chamber. This value gives a minimum base pressure of $\sim 10^{-5}$ Torr, easily obtainable with current MBE technology, where background pressures are typically on the order of $\sim 10^{-10}$ Torr [50].

Another major consideration is the issue of unintentional defect incorporation (dopants, traps, deep acceptors, etc.) as a consequence of low growth rates. An unintentional dopant monolayer deposition time of 10^5 times greater than that of a monolayer of material is necessary for negligible unintentional impurities. For a rare-earth titanate, such as $SmTiO_3$, a typical growth rate is 20 nm/hr. Assuming a sticking coefficient

of s = 1 for Sm, this gives a Sm flux of $\sim 10^{17}$ $m^{-2}s^{-1}$. This is approximately 35 s per monolayer of SmO. Then the time for a monolayer of unintentional dopants to accrue cannot be less than 35 s $\times$ 10^5 = 97.5 hrs. This corresponds with a minimum background pressure of $\sim 10^{-13}$ Torr (assuming carbon incorporation and a substrate temperature of 900 °C). Clearly, this requirement is not obtainable, but due to the low sticking coefficient of impurities at these substrate temperatures, high quality films of perovskite oxides have been and produced [52].

Hybrid MBE

A unique feature of the growth utilized throughout this work is the use of a metal-organic precursor element titanium tetraisopropoxide (TTIP) to supply Ti and oxygen. This circumvents the issue of very low fluxes from a Ti effusion source and the issue of trying to match fluxes to find a growth point. Using TTIP, dramatically higher growth rates are observed, going from $\sim$ 1 u.c./hr with a Ti effusion cell to $\sim$180 nm/hr [49]. Most importantly, the use of a metal-organic precursor allows for an adsorption limited growth regime, in which growth can be conducted with an overpressure of TTIP, where the stoichiometry will self-regulate within a range of flux ratios. This is due to the fact that TTIP is volatile and has a sticking coefficient of < 1. For a Ti effusion cell and growth of titanates, all constituents (including binary oxide adsorbate species) except oxygen have high sticking coefficients, leading to the grower seeking a growth point

instead of a growth window. Combining this with a very low growth rate makes it very easy to incorporate impurities (as discussed previously) as well as deviate from stoichiometry as a result of flux drift. Using a metal-organic circumvents these issues and has consistently yielded very high quality thin films. Indeed, using this method, world records have been set in low temperature mobility of La doped $SrTiO_3$ of 50,000 $cm^2V^{-1}s^{-1}$ [53].

2.3 Characterization methods

Common thin film characterization methods include *in situ* reflection high energy electron diffraction (RHEED), high resolution x-ray diffraction (XRD) and scanning transmission electron microscopy (STEM). The basics of these techniques will not be described in detail. The reader is encouraged to look elsewhere for details on the fundamentals of these characterization methods [54, 50]. Of central importance to this work is the use of magneto-transport as a tool to investigate different thin film properties. Basic transport methods can elucidate a great deal about a material, including mobility and scattering mechanisms [55], Fermi/non-Fermi liquid behavior [56] and quantum criticality [45], and magnetism [2]. In this section we give background to the basic technique and its practical application.

2.3.1 Hall and sheet resistance measurements

The primary phenomena that is utilized for transport measurements is the Hall effect, a result of the Lorentz force. An electron traversing a region with a perpendicular magnetic field relative to its direction of motion experiences a force normal to its direction and the field, described by

$$\mathbf{F}_{Lorentz} = q(\mathbf{E} + (\mathbf{v} \times \mathbf{B})) \tag{2.4}$$

where q is the electron charge, $\mathbf{E}$ and $\mathbf{B}$ the electric and magnetic fields and $\mathbf{v}$ the electron velocity.

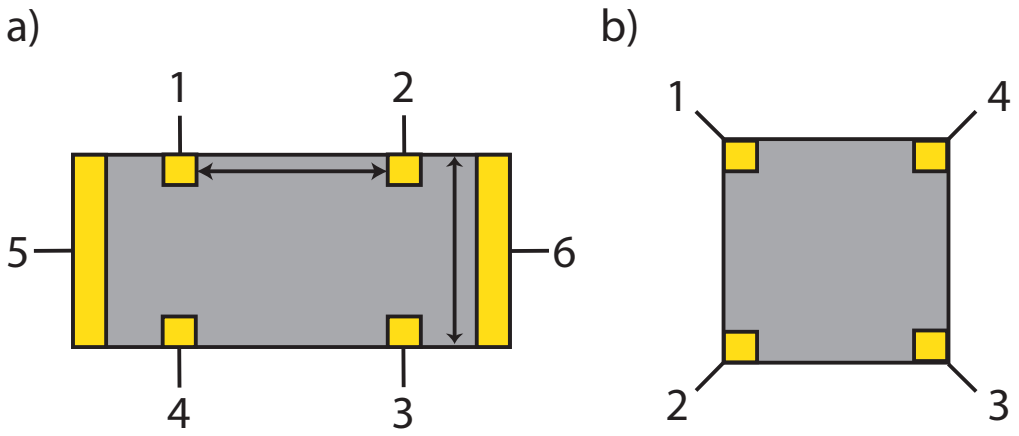

Figure 2.2: a) Hall bar and b) Van der Pauw contact geometries for transport measurements. The yellow regions are contacts, typically Ti/Au for the rare earth titanates, or Al/Ni/Au for $SrTiO_3$

If a current is passed through a sample experiencing a magnetic field normal to the plane of the current, the current is driven toward one edge of the sample. This leads to an accumulation of negative charges on one side of the sample and positive charges on the other, giving a potential difference. The voltage associated with this potential is the Hall voltage V_H.

The Hall voltage is related to the magnetic field *B*, current *I* and charge density n_s by

$$n_s = \frac{IB}{qV_H} = \frac{1}{qR_H} \tag{2.5}$$

where R_H is the Hall coefficient, given by the slope of the Hall resistance vs. magnetic field, $R_H = V_H/IB$, enabling a rather straightforward determination of the sheet carrier density. This can be further related to the mobility μ and sheet resistance R_s by

$$n_s = \frac{1}{q\mu R_s} \tag{2.6}$$

The mobility gives a quantitative measure of structural quality, as it is directly proportional to scattering mechanisms related to materials quality [55].

In practice, these quantities are determined in either Van der Pauw or Hall bar geometry (Figure 2.2). In Hall geometry (Figure 2.2a) a current is passed along the length of the bar and voltages are measured at points 1, 2, and 3. The Hall voltage is then

$V_H = V_2 - V_3$ and the Sheet resistance is $R_s = \frac{(V_1 - V_2)}{I}\frac{W}{L}$ where W and L are the width of the Hall bar and separation between contact pads, respectively.

In Van der Pauw, a geometry featured in Figure 2.2b is used, in which contacts are deposited in the corners of a square sample. Using this geometry, the sheet resistance can be calculated iteratively using the following expression

$$\exp \frac{-V_{43}/I_{12}}{R_S} + \exp \frac{-V_{14}/I_{23}}{R_S} = 1, \tag{2.7}$$

where V_{ij} and I_{ij} is the voltage and current between contacts i and j. The Hall voltage is given by V_{24} with current running from I_{13} [57].

2.3.2 Transport in magnetically ordered states

While transport cannot directly measure the magnetic state of a material, it can be used as an indirect method to probe a magnetically ordered state in an itinerant system. This can be done by probing the angular dependence of the transport with respect to a magnetic field. The quantity of interest is the magnetoresistance, given by

$$\Delta R = \frac{R(0) - R(B)}{R(0)}, \tag{2.8}$$

where R is expressed as a function of B. The angular dependence of the magnetoresistance is intimately related to the magnetic ordering in the material. There are different origins for changes in the angular dependence, and by measuring this and comparing

with models, we can gain insight into the magnetic structure of a material. Two possible origins of angular dependence are anisotropic magnetoresistance, experienced by a ferromagnetic metal, and spin Hall magnetoresistance, exhibited by paramagnetic metals in close proximity to a ferromagnetic insulator.

Anisotropic magnetoresistance (AMR) is a phenomena exhibited by *ferromagnetic* metals. The origin of AMR, first explained by Kondo [58], is found in spin-orbit coupling. Conduction electrons are scattered by the orbital angular momentum of electrons more tightly bound to the nucleus. Changing the orientation of magnetic field with respect to the sample acts to deform the more tightly bound electron cloud, thus changing the effective scattering cross section any mobile carrier experiences and the measured resistance. This is qualitatively illustrated in Figure 2.3.

Spin Hall magnetoresistance (SMR) occurs within paramagnetic metals that show strong spin-orbit coupling [59, 60, 61]. The spin Hall effect is the conversion of an electric current (J_e, see Figure 2.4) into a transverse spin current (J_s) resulting from spin-orbit scattering. Carriers scattered as a result of spin-orbit coupling are spin polarized, leading to an asymmetry in the scattered beam, and thus a spin current (analogous to the charge current in the Hall effect resulting from the Lorentz force, see Figure 2.4 a). The inverse spin Hall effect causes a portion of this spin current to be reflected at an interface (Figure 2.4 b), leading to an augmented electrical current $J_e^{'}$ (Figure 2.4 c). In the event that this interface is an insulating ferromagnet (such as $GdTiO_3$), then

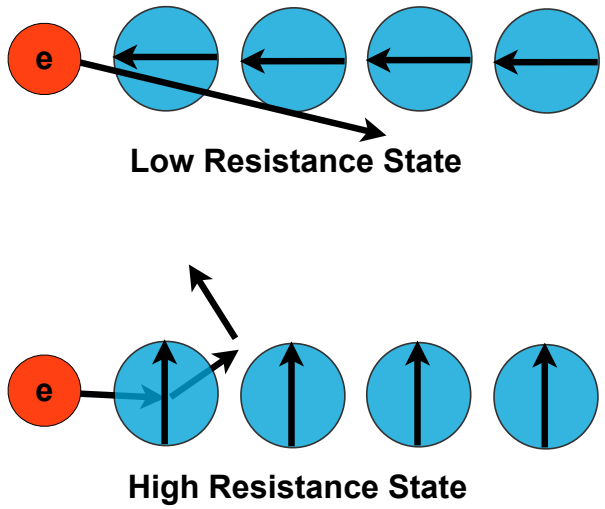

Figure 2.3: Qualitative illustration of high resistance (bottom) and low resistance (top) states.

the amount of reflected spin current will depend on the magnetization orientation in the ferromagnet **M**, as part can be absorbed as a spin transfer torque (Figure 2.4 d and e). Thus, similar to AMR, the angular dependence can elucidate the presence of spin Hall magnetoresistance.

If we define an angle α between the current and the magnetic field and an angle β between the magnetic field and the plane of the film (see Figure 2.5), then the expressions for the magnetization components in a cartesian system are

$$m_x = \cos(\alpha)\cos(\beta) \quad \text{and} \quad m_y = \sin(\alpha)\cos(\beta) \tag{2.9}$$

and the expressions for longitudinal (ρ_{xx}) and transverse (ρ_{xy}) magnetoresistance for SMR are given by

$$\rho_{xx} = \rho_0 - \Delta\rho_S m_y^2 \quad \text{and} \quad \rho_{xy} = \Delta\rho_S m_x m_y \tag{2.10}$$

where ρ_0 is a constant offset and $\Delta\rho_S$ is the resistivity change from the SMR. For AMR, the longitudinal (ρ_{xx}) and transverse (ρ_{xy}) magnetoresistance expressions are given by

$$\rho_{xx} = \rho_\perp - \Delta\rho_A m_x^2 \quad \text{and} \quad \rho_{xy} = \Delta\rho_A m_x m_y \tag{2.11}$$

where $\Delta\rho_A = \rho_\parallel - \rho_\perp$ ($\rho_\perp$ and $\rho_\parallel$ are the resistivity with magnetic field perpendicular and parallel to the current, respectively) [59]. It is clear from the above formula that these two phenomena can be easily distinguished through a qualitative analysis of the longitudinal magnetoresistance. We simply need to look at the behavior of ρ_{xx} and determine weather it is a function of m_x or m_y.

These transport features, which can elucidate magnetic properties of a material, can be correlated with other magnetic measurements, such as SQUID (superconducting quantum interference device) magnetometry, which gives thin film magnetization as a function of temperature and magnetic field. This and the aforementioned angular dependent magnetoresistance will be discussed in greater detail in Chapter 4.

2.3.3 Strongly correlated behavior in transport

Fermi liquid theory

In Fermi liquid theory, correlated electrons that interact via Columbic interactions are treated as quasiparticles. The theory asserts that if the interactions are adiabatically turned on in a many-body system, eigenstates evolve smoothly from non-interacting states to interacting states of the correlated system. This results in a one-to-one correspondence between non-interacting and interacting eigenstates, preserving certain quantum numbers such as charge and spin, while others must be renormalized, such as mass and magnetization. In transport, correlation effects and the presence of a Fermi liquid (or the lack there of) can be ascertained by the temperature dependence of the resistivity [62, 63].

From the Drude conductivity, the resistivity is given by

$$\rho = \frac{m^*}{ne^2\tau}, \tag{2.12}$$

where m^* is the effective mass, n the carrier density and τ the scattering time. The scattering time will determine the temperature dependence of the resistivity. To understand the temperature dependence of τ, we begin a thought experiment with temperature T = 0. Scattering occurs between a charge above and a charge below the Fermi energy. Pauli exclusion dictates that the resultant energy be above the Fermi energy, while con-

servation of energy does not allow the total energy to exceed that of the higher energy electron E_1, i.e. $\Delta E = E_1 - E_F$. Under these constraints, Fermi's Golden Rule results in a decay rate $1/\tau \propto \Delta E^2$. At T > 0, an additional contribution to the scattering rate originates from thermal excitation $k_B T$. This term is also proportional to the number of available states, and thus by the same argument above, the decay rate is inversely proportional to the temperature, $1/\tau \propto T^2$. From the Drude conductivity relation, we have $\rho \propto T^2$ [63]. More specifically,

$$\rho(T) = \rho_0 + AT^2 \tag{2.13}$$

where $\rho(T)$ is the temperature dependent resistivity, ρ_0 the residual resistivity from impurity scattering, and A a coefficient proportional to the effective mass [64]. Thus, a transport measurement that follows a T^2 dependence is a strong indication of correlation effects.

Quantum critical behavior

Many correlated material systems, such as high-T$_c$ superconductors [18], show deviations from Fermi liquid behavior in a systematic fashion. This deviation is seen in close proximity to a quantum phase transition, where quantum fluctuations alter the nature of the electronic quasiparticles, resulting in non-Fermi liquid behavior [63, 65]. The deviation from Fermi liquid behavior often follows a specific temperature depen-

dence and is a function of dimensionality and any incipient magnetic order present in the system [19]. Thus, by detecting systematic deviations from Fermi liquid behavior in transport, the presence and proximity to a quantum critical point can by inferred. In Chapter 5, we demonstrate quantum critical behavior in oxide heterostructures.

2.4 Chapter summary

In this chapter, we introduced the basic methods used to produce and characterize the novel structures of interest throughout this work. Our focus was on establishing the importance of MBE and the unique advantages in using a hybrid metal-organic approach. We then discussed the various ways in which transport can elucidate the properties of these unique structures.

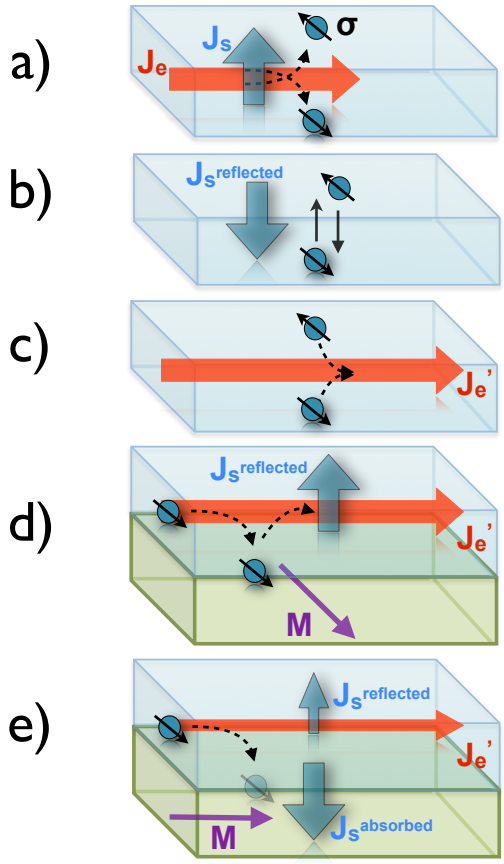

Figure 2.4: Figure illustrating the physical mechanism behind spin Hall magnetoresistance. The blue region is the paramagnetic metal with spin orbit coupling and the green region is a ferromagnetic insulator. Parts a), b) and c) illustrate spin Hall and inverse spin Hall effects, while d) an e) illustrate how the current will then depend on the magnetization orientation of the ferromagnet.

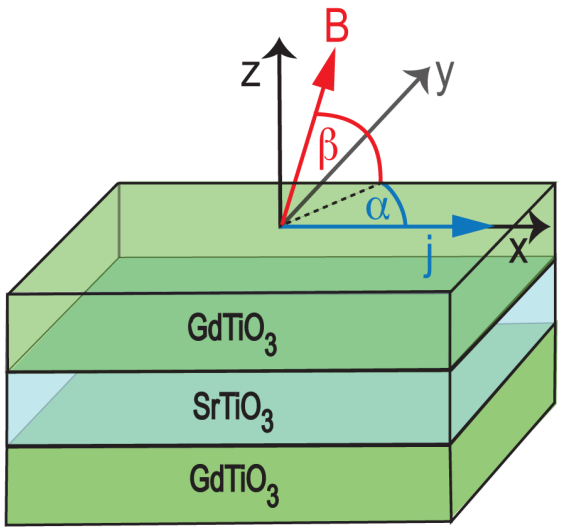

Figure 2.5: Schematic of the measurement geometry, where **j** indicates the current, α is the angle between **B** and **j**, and β is the angle between **B** and the film plane. The illustrated structure is a $SrTiO_3$ quantum well sandwiched between two $GdTiO_3$ layers. Reproduced from Ref [2] with permission from the American Physical Society, Copyright 2013.

Chapter 3

Structural Distortions, Magnetism and Transport

3.1 Introduction

To understand the underlying physics of heterostructures composed of Mott materials and band insulators (the relative roles of disorder, correlation effects, and interactions of the carriers with the structure) it is informative to explore if the magnetization (in the case of $GdTiO_3$) and electrical transport (for $SrTiO_3$ quantum wells) can be systematically tuned by adjusting the external parameters of the system. Strain in epitaxially mismatched heterostructures and the need for connectivity of the oxygen octahedra at an interface offer a unique way of tuning octahedral distortions without the need for changing the chemical composition [66, 67]. This provides a way of controlling orbital-lattice coupling, and an avenue for insight into the properties of materials not possible in their bulk state. In this chapter, we discuss structure-transport and structure-magnetism correlations in heterostructures composed of $GdTiO_3$/$SrTiO_3$ and $SmTiO_3$/$SrTiO_3$.

Introduced in Chapter 1, $GdTiO_3$ and $SmTiO_3$ are Mott insulators, with a d^1 electron configuration. They both have the same parent orthorhombic crystal structure, but with slightly different octahedral distortions ($SmTiO_3$ being the smaller of the two) [43]. $GdTiO_3$ is ferrimagnetic while $SmTiO_3$ is antiferromagnetic [1], a result of their different orbital ordering [39, 44, 37]. In the first section, we discuss the relationship

Parts of this chapter are reprinted with permission from Jack Y. Zhang, **Clayton A. Jackson**, Santosh Raghavan, Jinwoo Hwang, and Susanne Stemmer, PRB **88** 121104(R) (2013), copyright 2013 and from Jack Y. Zhang, **Clayton A. Jackson**, Ru Chen, Santosh Raghavan, Pouya Moetakef, Leon Balents and Susanne Stemmer, PRB **89** 075140 (2014), copyright 2014 by the American Physical Society.

between magnetism and structural distortion in $GdTiO_3$. In the second section, we discuss the role of distortions in conducting $SrTiO_3$ quantum wells.

3.2 Magnetism in thin $GdTiO_3$

As discussed briefly in Chapter 1, magnetic ordering is related to distortions and tilts of the Ti-O octahedra in the orthorhombic $GdFeO_3$ structure. There are two types of orbital ordering, ferro-orbital and antiferro-orbital. Both are compatible with *Pbnm* symmetry [37, 38, 39, 40, 41, 42] of the $GdFeO_3$ structure. Ferro-orbital ordering is concomitant with smaller distortions and favors antiferromagnetic ordering (AFM), while antiferro-orbital ordering favors ferromagnetic order (FM) and larger distortions.

In Glazer notation, the $GdFeO_3$ structure is characterized by $a^-a^-b^+$ type tilting [68]. The x and y degrees of freedom allow the A-site cations to shift to a more energetically favorable state. The degree of displacement is a function of the geometry [69]. The amount of $GdFeO_3$-type distortion changes systematically with the transition from AFM to FM ordering, and the ordering temperature [70, 71, 43, 1], but the relative roles of orbital-lattice coupling and structural distortions remain an open topic [39, 43, 72, 73]. It has been shown that film thickness correlates with the degree of octahedral tilt for thin films [74].

For $GdTiO_3$, the ferromagnetic Ti complex couples antiferromagnetically to the moment from the Gd, yielding a net ferrimagnetic state [43, 1, 75]. The AFM Gd-O-Ti interactions are believed to be weaker than the ferromagnetic Ti-O-Ti interactions [43]. $GdTiO_3$ is just on the FM side of the FM-AFM phase boundary; therefore, if the FM character is sensitive to octahedral rotations and distortions, significant effects on its magnetism with structural modifications may be expected.

3.2.1 Sample structure and measurement

All structures were grown on (001) $(La0_{0.3}Sr_{0.7})(Al_{0.65}Ta_{0.35})O_3$ (LSAT) by hybrid MBE [76, 8]. A 20 nm $GdTiO_3$ film was grown directly on LSAT, while $GdTiO_3$ layers of 3.5 nm, 2.4 nm, and 2.0 nm thickness (10, 7, and 6 GdO layers, respectively) were grown in a superlattice structure with 5 nm $SrTiO_3$ spacers. Superlattices contained either 5 or 10 $GdTiO_3$ layers, and thus approximately the same amount of $GdTiO_3$, by volume, as the 20 nm sample. All superlattice structures had 10 nm $SrTiO_3$ substrate buffers and caps, respectively.

The magnetization was measured in a SQUID magnetometer with the magnetic field in the plane of the film. The magnetic measurements were correlated with structural distortions, characterized with transmission electron microscopy, discussed in more detail elsewhere [74, 3, 4].

3.2.2 Effects of structural distortion on magnetism

Figure 3.1a shows the magnetization of each sample as a function of temperature under a constant field of 100 Oe. The magnetization hysteresis at 2 K is shown in Figure 3.1b. The measured magnetization includes the diamagnetic and paramagnetic responses from the $SrTiO_3$ layers, the LSAT and a Ta backing layer. Because of the superlattice structure, isolation of the $GdTiO_3$ response could not be done. Thus, conclusions about saturation magnetization or other parameters that depend on the volume should not be drawn from this data set. However, the Curie temperature (T_c) and coercivity are properties of only the FM $GdTiO_3$.

Analysis of Figure 3.1 reveals that the reduction in film thickness (which correlates with octahedral distortion [3, 74, 4] correlates with a decrease in T_c. The T_c of the 20 nm film ($\sim$ 30 K) agrees well with the bulk [43, 1, 75]. All $GdTiO_3$ layers with thicknesses greater than 2.0 nm are FM, but their T_c decreases monotonically with decreasing thickness. The FM ground state only vanishes in the 2.0 nm film. This behavior is expected by analogy with the bulk rare earth titanates, which show a decrease in T_c with increasing bandwidth (concomitant with reduced distortions), similar to what is observed in band ferromagnetism [7].

The results suggest a picture of a direct interaction between orbital ordering and the lattice. Recent reports of structural anomalies at the magnetic ordering temperature, which also support a direct lattice-orbital coupling [43], agree with this result. Oth-

ers have found that in the AFM rare earth titanates, the orbital ordering changes at the ordering temperature, also suggesting a direct interaction [39]. The FM rare-earth titanates thus appear to closely match models of insulating magnetic systems [77, 78, 79]. In these systems, antiferro-orbital ordering in conjunction with exchange results in ferromagnetism at a temperature below the orbital ordering temperature. The $4f^7$ configuration of the Gd ions ensures no orbital angular momentum contributions from the Gd, suggesting the interatomic exchange field, even at lower Ti-O-Ti bond angles, favors the FM ground state.

3.3 Transport in thin $SrTiO_3$ quantum wells

In this section, we compare transport with structure for $SmTiO_3$/$SrTiO_3$/$SmTiO_3$ and $GdTiO_3$/$SrTiO_3$/$GdTiO_3$ heterostructures. In both cases, the $SrTiO_3$ quantum wells contain a two-dimensional electron gas on the order of $\sim 7 \times 10^{14}$ cm^{-2} [80, 81]. $SrTiO_3$ quantum wells embedded in $GdTiO_3$ show a metal-insulator transition when their thickness is reduced such that they contain only two SrO layers [80]. At these dimensions, the electron system is localized and the resistivity increases by several orders of magnitude. Metal-insulator transitions at reduced thicknesses have also been seen in thin quantum wells and films of many other perovskite materials, such as $SrVO_3$ [82], $LaNiO_3$ [83, 84, 85], and $NdNiO_3$ [86]. For many d-electron systems, the breaking

of symmetry of spin and orbital degrees of freedom play a pivotal role in creating an insulating state [30]. Transition metal-oxygen octahedral tilts that reduce the symmetry relative to the parent cubic perovskite structure are modified in quantum wells due to film strain [87, 88] and interfacial coherency [89, 66, 67, 90].

3.3.1 Sample structure and measurement

All films were grown by hybrid MBE [8, 76] on (001) LSAT substrates. Electrical transport measurements were carried out on $SrTiO_3$ quantum wells embedded in $GdTiO_3$ and $SmTiO_3$, respectively (see chapter on Methods). The $GdTiO_3$ and $SmTiO_3$ layers were 4 and 10 nm thick, respectively (See Figure 3.2). The thicknesses of the $SrTiO_3$ quantum wells are specified in terms of the number of SrO layers, as verified by transmission electron microscopy (TEM) by Jack Zhang. Electrical contacts, consisting of a 40 nm Ti and 400 nm Au top layer, were deposited by electron beam evaporation in van der Pauw geometry. A Physical Property Measurement System (Quantum Design PPMS Dynacool) was used for resistivity and Hall measurements.

3.3.2 Electrical transport analysis

Figure 3.2 shows the sheet resistances as a function of $SrTiO_3$ quantum well thickness and temperature. Metallic behavior is observed for all quantum wells in $SmTiO_3$, down to a single SrO layer. In contrast, quantum wells embedded in $GdTiO_3$ are metal-

lic for thicknesses greater than two SrO layers, but become insulating for 1 and 2 SrO layers.

The results provide insight into the correlation physics of the perovskite titanates. An increase in the effective 3D density, as well as changes in octahedral tilts and reduced Ti-O-Ti bond angles [74, 3, 4] correlate with the transition to the insulating state and occur only in the quantum wells embedded in $GdTiO_3$. A crossover from large to small polaron transport occurs in the lightly-doped, insulating rare earth titanates between $SmTiO_3$ and $GdTiO_3$ [1]. The electrons in the insulating quantum wells of $SrTiO_3$ in $GdTiO_3$ form a high-density small polaron gas [91]. In contrast to the localization in the $SrTiO_3$ embedded in $GdTiO_3$, quantum wells embedded in $SmTiO_3$ are metallic for all $SrTiO_3$ layer thicknesses. Symmetry-lowering structural distortions, measured by quantifying the Sr-column displacements, are present in the insulating quantum wells, but are either absent or very weak in all metallic quantum wells, independent of whether they are embedded in $SmTiO_3$ or in $GdTiO_3$ [4].

3.4 Chapter summary

In this chapter, transport and magnetism of heterostructures composed of $SrTiO_3$, $SmTiO_3$ and $GdTiO_3$ layers were studied. In the case of thin $GdTiO_3$ embedded in $SrTiO_3$, ferromagnetism is suppressed as the $GdTiO_3$ layers become thinner, and is

gone entirely at 2 nm. The results indicate that the FM ground state is controlled by the narrow bandwidth, exchange and orbital ordering. For $SrTiO_3$ embedded in $SmTiO_3$ and $GdTiO_3$, a decrease in film thickness, which relates to the degree of distortion in the film [4], corresponds with a metal-insulator transition if the material in which it is embedded has sufficient distortion, made evident in comparing $SmTiO_3/SrTiO_3/SmTiO_3$ and $GdTiO_3/SrTiO_3/GdTiO_3$ heterostructures.

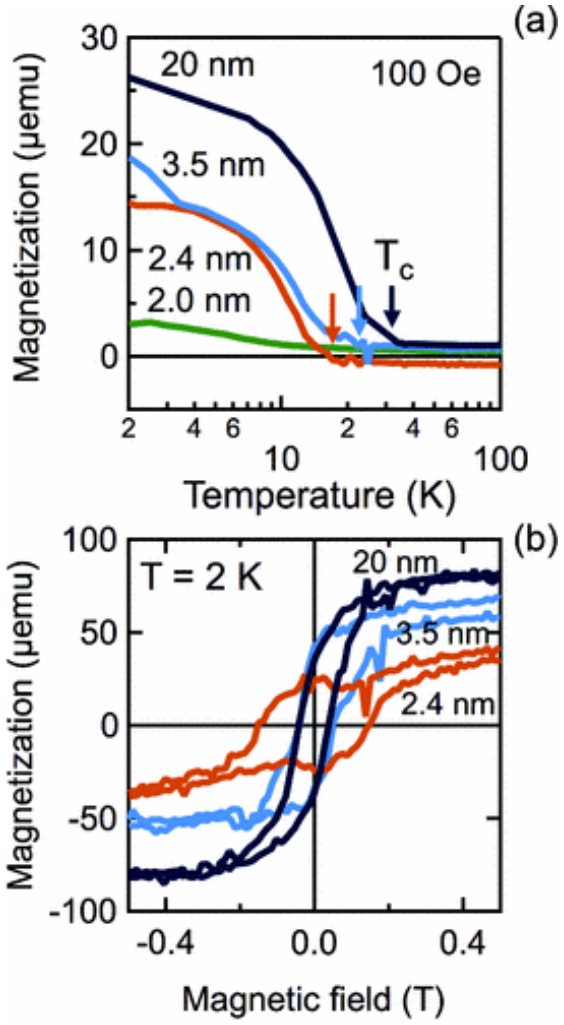

Figure 3.1: **(a)** Field-cooled magnetization as a function of temperature for samples with $GdTiO_3$ films of various thicknesses under a magnetic field of 100 Oe. The Curie temperature T_c is indicated by the arrows. **(b)** Magnetization as a function of magnetic field. Reprinted with permission from Jack Y. Zhang, **Clayton A. Jackson**, Santosh Raghavan, Jinwoo Hwang, and Susanne Stemmer, PRB **88** 121104(R) (2013), copyright 2013 by the American Physical Society (Ref. [3]).

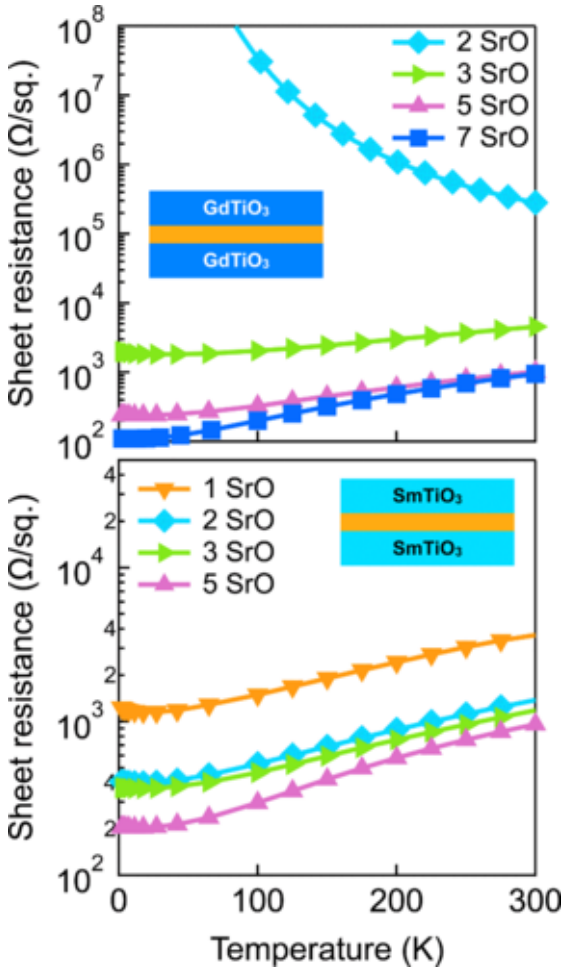

Figure 3.2: Temperature dependent sheet resistance for $SmTiO_3/SrTiO_3/SmTiO_3$ **(bottom)** and $GdTiO_3/SrTiO_3/GdTiO_3$ **(top)** heterostructures. Reprinted with permission from Jack Y. Zhang, **Clayton A. Jackson**, Ru Chen, Santosh Raghavan, Pouya Moetakef, Leon Balents and Susanne Stemmer, PRB **89** 075140 (2014), copyright 2014 by the American Physical Society (Ref. [4]).

Chapter 4

Interface-Induced Magnetism in Complex Oxide Heterostructures

4.1 Introduction

Interfacial proximity effects between Mott/band insulators have attracted attention for their potential utilization in spintronics, quantum computing, and the observation of Majorana fermions [92, 93, 94]. Oxide heterostructures are attractive for inducing phenomena through interfacial proximity, because the relevant phenomena, such as superconductivity, high density 2DEGs, spin-orbit coupling [95, 96, 97, 98] (a result of a breaking of inversion symmetry in the 2DEG) and magnetism can all be found in a single materials class, the perovskites. This allows for high-quality epitaxial heterostructures.

Heterostructures composed of $SrTiO_3$, $SmTiO_3$ and $GdTiO_3$ are excellent candidate materials in which to look for and exploit proximity effects, due to the rare earth titanates magnetic properties, and the presence of the interfacial high density 2DEG with 3×10^{14} cm^{-2} mobile carriers in the $SrTiO_3$ [81, 45] (discussed in more detail in Chapter 1). Thin (< 2 nm) quantum wells of $SrTiO_3$ embedded in $GdTiO_3$ show magnetoresistance hysteresis at low temperatures (See Figure 4.1 and [5]).

The ferromagnetic properties of the quantum well are clearly distinct from those of the $GdTiO_3$. As can be seen in Figure 4.2 (Reference [5]), the coercive field of the $GdTiO_3$ at 2 K is about 0.02 T . The coercivity of the quantum well, which we associate

Parts of this chapter are reprinted with permission from **Clayton A. Jackson** and Susanne Stemmer, Physical Review B **88**, 180403(R) (2013), copyright 2013 by the American Physical Society.

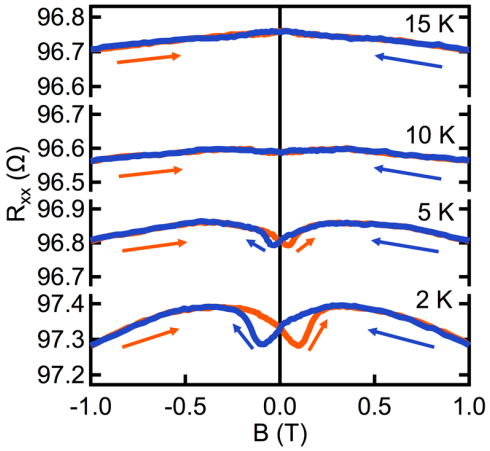

Figure 4.1: Longitudinal magnetoresistance for a 4 nm $GdTiO_3$/ 0.8 nm $SrTiO_3$/ 4 nm $GdTiO_3$ sample. The magnetic field is in the plane of the film and orthogonal to the current. Reprinted with permission from **Clayton A. Jackson** and Susanne Stemmer, Physical Review B **88**, 180403(R) (2013), copyright 2013 by the American Physical Society (Ref [2]).

with the minimum in the magnetoresistance hysteresis, appears at a much larger field, around 0.1 T. The onset of hysteresis in the quantum wells occurs between 5 and 10 K, whereas the Curie temperature of the 4 nm $GdTiO_3$ is $\sim$ 20 K. We also note that ferromagnetism and metallic conduction do not coexist in the rare earth titanates [99]. Octahedral distortions, a requirement for ferromagnetism in the insulating rare earth titanates [100], do not appear until the quantum wells are thinner than those investigated here, and insulating [74].

It was conjectured that the hysteresis could be a result of proximity to the ferrimagnetic $GdTiO_3$, but study of the magnetic state of the $SrTiO_3$ was not conclusive. It is possible that the magnetism in the $SrTiO_3$ is due to exchange coupling across the in-

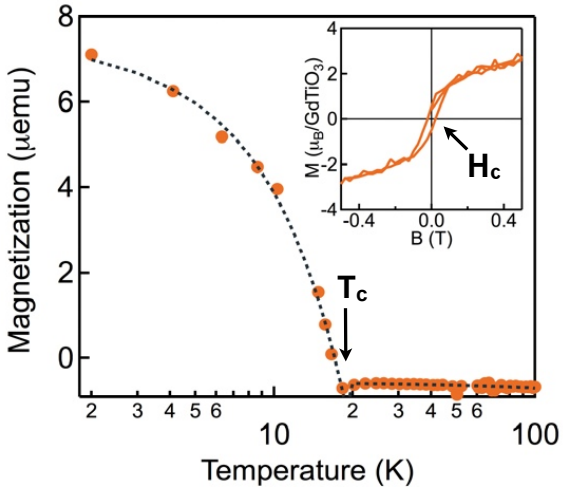

Figure 4.2: Magnetization as a function of temperature at 10 mT for a 4 nm $GdTiO_3$/ 1 nm $SrTiO_3$/ 4 nm $GdTiO_3$ heterostructure. The dotted line is a guide to the eye. The inset shows the magnetization M as a function of magnetic field at 2 K. Reprinted figure with permission from Pouya Moetakef, James R. Williams, Daniel G. Ouellette, Adam P. Kajdos, David Goldhaber-Gordon, S. James Allen, and Susanne Stemmer, Physical Review X 2, 021014 (2012), copyright 2013 by the American Physical Society (Ref [5]) [doi].

terface. Theoretical calculations show that thin quantum wells tend towards ferromagnetism [89, 12]. In this case, the $SrTiO_3$ quantum well may exhibit anisotropic magnetoresistance (AMR), typical of ferromagnets. An alternative explanation is that the resistance hysteresis is a function of the magnetization orientation in $GdTiO_3$, without the $SrTiO_3$ quantum well itself being ferromagnetic. The latter is a consequence of direct and inverse spin Hall effects, called spin Hall magnetoresistance (SMR) [59, 60, 61]. Spin-orbit coupling is central to both SMR and AMR (see Methods Chapter). It is known that spin related effects are evident in $SrTiO_3$ 2DEGs [98, 101]. Thus, it is

possible for either AMR (for a ferromagnetic quantum well) or SMR (for a paramagnetic quantum well) to occur. The two phenomena are distinguishable by the angular dependence of the magnetoresistance on the orientation of the magnetic field [59].

4.2 Sample structure and measurement

$GdTiO_3/SrTiO_3/GdTiO_3$ and $SmTiO_3/SrTiO_3/SmTiO_3$ quantum well structures were grown by hybrid molecular beam epitaxy on (001) LSAT crystals. The $GdTiO_3$ based quantum wells consisted of 4 nm top and bottom $GdTiO_3$ layers, and 0.8 nm $SrTiO_3$ (about three SrO layers [74]). The sample structure is featured in Figure 2.5. In contrast to $GdTiO_3$, which is ferrimagnetic with a Curie temperature of $\sim$ 30 K in bulk [1] and $\sim$ 20 K in the samples with 4 nm $GdTiO_3$ [5], $SmTiO_3$ is antiferromagnetic with a Néel temperature of $\sim$ 50 K [43]. Electrical and structural characterization, as well as growth details are described in Chapter 2 and elsewhere [5, 74, 102, 76]. The carrier mobility was an order of magnitude higher than in conducting, doped $GdTiO_3$ or $SmTiO_3$, indicating that electrical transport occurs only in the $SrTiO_3$ quantum well. Further evidence comes from magnetotransport, $SrTiO_3$-like Seebeck values [103], and band offsets that favor charge transfer into the $SrTiO_3$ [81, 46].

40 nm Ti/400 nm Au electrical contacts were deposited by electron beam evaporation in van der Pauw geometry with a shadow mask, with the Au contact being

the topmost layer. Hall and Magnetoresistance data were collected using a Physical Property Measurement System (Quantum Design PPMS Dynacool). The system's resistivity option was used for Hall and sheet resistance and the electrical transport option for magnetoresistance. The latter utilizes an internal lock-in technique. For this measurement, a frequency of 70.1 Hz and an averaging time of 20 s per measurement were used. An external junction box allows assigning any function to any contact pad using external cables, and was used to confirm that the same behavior was measured within each possible contact geometry for a specific measurement geometry. The magnetoresistance was measured between $\pm$ 1 T, pausing every 0.016 T to collect data using the internal lock-in. The sweep rate between data collection points was 0.015 T/s. Multiple sweep rates were used in the measurement and no noticeable difference was detected. Longer averaging times showed no appreciable change in the measured resistance. The angular dependence of the magnetoresistance was characterized by varying the angles α and β between the current, **j**, and the magnetic field, **B**. As shown in Figure 2.5, α lies in the film plane (α = 0° for **B** and **j** parallel), while β is the angle between the film plane and **B** (β = 0° if **B** lies in the film plane). A horizontal rotator was used to vary β. The angle α was set to 0° or 90° by rotating the external leads and to 45° by adjusting the placement of the sample on the mounting puck.

Contrary to what is expected for weak localization of a two-dimensional system, the longitudinal magnetoresistance (R_{xx}) of all samples was negative at low temperatures,

independent of whether the field was in or out of plane. Negative magnetoresistance can, however, also be due to ferromagnetism or antiferromagnetism of the 2DEG [104, 105]. As can be seen in comparing the magnetoresistance of $GdTiO_3/SrTiO_3/GdTiO_3$ and $SmTiO_3/SrTiO_3/SmTiO_3$ (Figures 4.3 and 4.5, respectively) only the $GdTiO_3$ containing samples exhibited magnetoresistance hysteresis, superimposed on the negative R_{xx} background. As can be seen in Figure 4.1, the onset temperature for the hysteresis is between 5 and 10 K. From the direct comparison of the magnetoresistance for the $SmTiO_3$ and $GdTiO_3$ based structures, we can conclude that the presence of the ferrimagnetic $GdTiO_3$ is a necessary requirement for ferromagnetism in these samples.

4.3 Angular dependence of the magnetoresistance

Figure 4.3 shows the relative changes of longitudinal magnetoresistance ΔR_{xx} and transverse magnetoresistance ΔR_{xy} (where $\Delta R_{ij} = R_{ij}(B) - R_{ij}(0)$), respectively, for the $GdTiO_3/SrTiO_3/GdTiO_3$ quantum well structure for three different values of α, at $\beta = 0^\circ$. Hysteretic behavior is observed for all α, except for $\alpha = 0^\circ$ in the planar Hall geometry. Both the transverse and the longitudinal hysteresis show a reversal from peak to dip with α. The relative changes are larger in R_{xy}, where the peak for $\alpha = 45^\circ$ corresponds to a $\sim 20\%$ change. The absolute changes were comparable, less than 1 Ω for both R_{xy} and R_{xx}.

As discussed in Chapter 2, we can distinguish between SMR and AMR by measuring the longitudinal and transverse magnetoresistance, (R_{xx}) and R_{xy}, where $R_{ij} \propto \rho_{ij}$)), and comparing the data with the following expressions [59, 89, 106].

$$\text{SMR:} \quad \rho_{xx} = \rho_0 - \Delta\rho_S m_y^2 \quad \text{and} \quad \rho_{xy} = \Delta\rho_S m_x m_y \tag{4.1}$$

$$\text{AMR:} \quad \rho_{xx} = \rho_\perp - \Delta\rho_A m_x^2 \quad \text{and} \quad \rho_{xy} = \Delta\rho_A m_x m_y \tag{4.2}$$

where ρ_{xx} and ρ_{xy} are the longitudinal and transverse resistivities, ρ_0 is a constant offset, $\Delta\rho_S$ the resistivity change from the SMR, $\Delta\rho_S = \rho_\parallel - \rho_\perp$, where $\rho_\perp$ and $\rho_\parallel$ are the resistivity with magnetic field perpendicular and parallel to the current, respectively.

The magnetization orientations are

$$m_x = \cos(\alpha)\cos(\beta) \quad \text{and} \quad m_y = \sin(\alpha)\cos(\beta) \tag{4.3}$$

Comparing these expressions with the data featured in Figures 4.3 and 4.4, it is clear that R_{xx} for β = 0° does not behave according to the SMR effect, because R_{xx} should be maximized for α = 0° and minimized for α = 90°, as $\Delta\rho_S > 0$ always applies [89]. The experimental behavior instead shows that, at large fields, when the magnetization should be parallel to **B**, R_{xx} decreases for α = 0° and increases for α = 90° (see Figure 4.3a). R_{xx} at β = 0° follows AMR behavior with $\Delta\rho_A < 0$, for which the resistance

should be maximized for α = 90° and minimized for α = 0°. R_{xy} at β = 0° is also consistent with AMR and $\Delta\rho_A < 0$. In this case, R_{xy} should be maximized (positive) for α = 135°, minimized (negative) for α = 45°, and zero for α = 0°, exactly as is observed, as can be seen in Figure 4.3b.

The two effects can be further distinguished by rotating the magnetization out of plane while measuring the change in resistance at a fixed α. Figure 4.4 shows the β-angle dependence of R_{xx} for α = 0° and α = 90°, respectively, at three different values of B. For AMR, $\Delta\rho_A < 0$, and α = 0° we expect a cosine dependence on β, with R_{xx} increasing, as β is increased, which is observed when B exceeds the demagnetization field, evident in Figure 4.4a. In contrast, for SMR, R_{xx} should be independent of β for α = 0°.

The behavior at α = 90° is more complicated, because it shows a β-angle dependence. For AMR and α = 90°, R_{xx} should be independent of β. It is, however, also inconsistent with SMR, for which changing β away from 0° should cause R_{xx} to increase. It is likely the anisotropy in R_{xx} at α = 90° reflects the two-dimensionality of the system, which may also contribute to the offset seen for α = 0°, i.e., the minimum of R_{xx} is shifted slightly from β = 0°.

Data from the $SmTiO_3/SrTiO_3/SmTiO_3$ quantum well structure is featured in Figure 4.5. This structure also shows a decrease in R_{xx} as β is changed from 0° to 90° for α = 90°, confirming that the anisotropy is independent of ferromagnetism.

4.4 Ferromagnetism in $SrTiO_3$ quantum wells

The occurrence of AMR is consistent with an emergent conducting ferromagnetic state in the $SrTiO_3$ quantum well embedded in the $GdTiO_3$ based structures. The results also demonstrate the importance of spin-orbit coupling in these $SrTiO_3$ quantum wells, which is necessary for AMR. The ferromagnetism is related to the magnetic state of the $GdTiO_3$ and is likely a result of exchange coupling, as it does not appear in quantum wells bound by $SmTiO_3$. The origin of the negative AMR ($\Delta\rho_A < 0$) requires further investigations into the microscopic mechanisms responsible. The negative AMR is also observed in compressively strained, two-dimensional, magnetic III-V semiconductors [107]. We note that the $SrTiO_3$ quantum wells are under compressive strain from the LSAT substrate. No anomalous Hall effect could be detected (see Figure 4.6), likely because the AMR is relatively weak.

4.5 Chapter summary

In this chapter we investigated the angular dependence of the magnetoresistance of thin (< 1 nm), metallic $SrTiO_3$ quantum wells epitaxially embedded in insulating, ferrimagnetic $GdTiO_3$ and insulating, antiferromagnetic $SmTiO_3$. We showed that the longitudinal and transverse magnetoresistance in the structures with $GdTiO_3$ are consistent with anisotropic magnetoresistance, and thus indicative of induced ferromag-

netism in the $SrTiO_3$, rather than a non-equilibrium proximity effect. Comparison with the structures with antiferromagnetic $SmTiO_3$ showed that the properties of thin $SrTiO_3$ quantum wells can be tuned to obtain magnetic states that do not exist in the bulk material.

These results provide an incentive for future theoretical and experimental studies that examine the influence of different parameters such as exchange, orbital character and carrier density on the magnetism, its dependence on the thickness of the quantum well, and its microscopic nature [100]. The structures show an emergent phenomenon, namely, evidence of a metallic ferromagnetic state, that is a result of multiple components of the system (dimensionality, the high density 2DEG, and the magnetic ordering of $GdTiO_3$) and show potential for combining correlated phenomena and engineering novel states of matter. In the following chapter, we will examine in more detail the effect of antiferromagnetic $SmTiO_3$ in these quantum well structures.

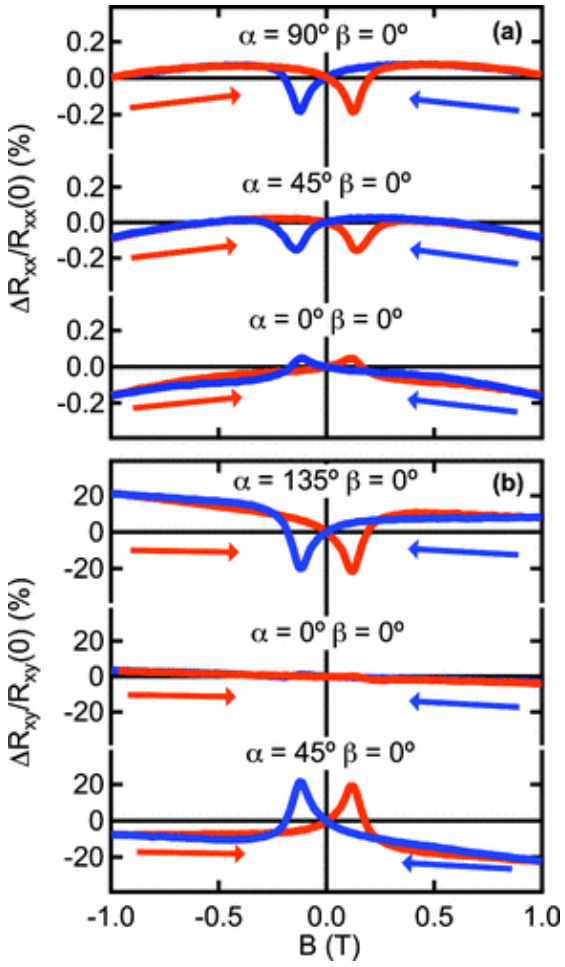

Figure 4.3: **(a)** Relative changes in the longitudinal magnetoresistance as a function of in-plane angle α at $\beta = 0°$. **(b)** Relative changes in the transverse magnetoresistance as a function of in-plane angle α at $\beta = 0°$. Reprinted with permission from **Clayton A. Jackson** and Susanne Stemmer, Physical Review B **88**, 180403(R) (2013), copyright 2013 by the American Physical Society (Ref [2]).

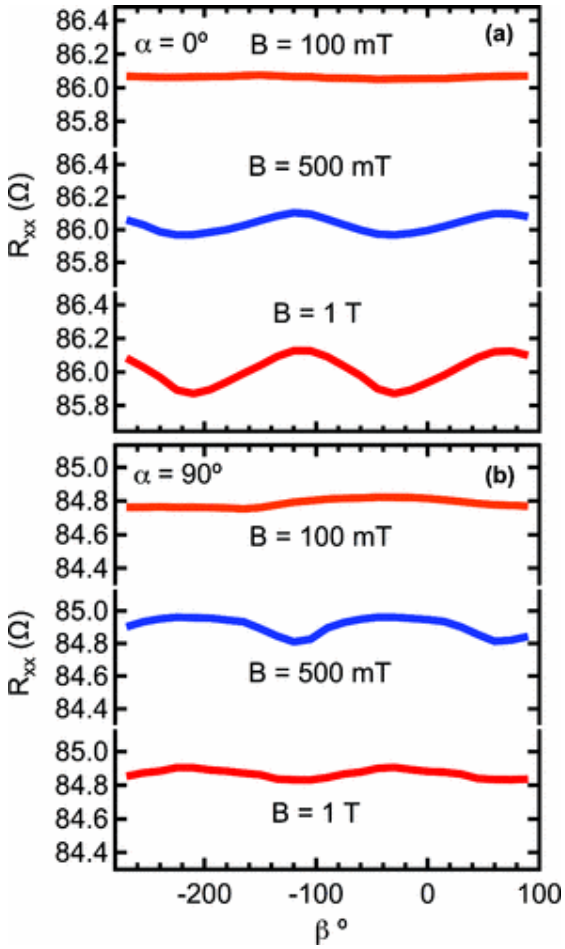

Figure 4.4: β dependence of R_{xx} at magnetic fields of .1, .5 and 1 T for **(a)** $\alpha = 0°$ and **(b)** $\alpha = 90°$. Reprinted with permission from **Clayton A. Jackson** and Susanne Stemmer, Physical Review B **88**, 180403(R) (2013), copyright 2013 by the American Physical Society (Ref [2]).

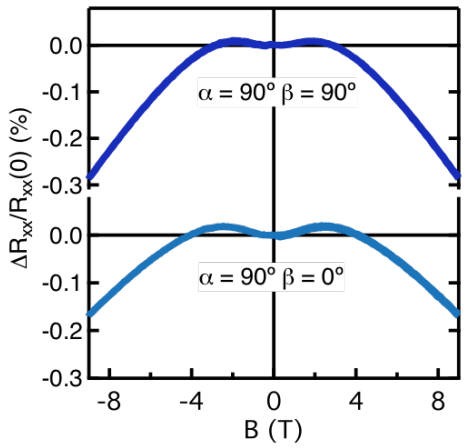

Figure 4.5: Relative changes in R_{xx} for a $SmTiO_3/SrTiO_3/SMTiO_3$ heterostructure. The $SmTiO_3$ layer thicknesses are 10 nm and the $SrTiO_3$ layer thickness is 0.4 nm. The field was swept from +9 to -9 and back to +9 T. No hysteresis is observed. Reprinted with permission from **Clayton A. Jackson** and Susanne Stemmer, Physical Review B **88**, 180403(R) (2013), copyright 2013 by the American Physical Society (Ref [2]).

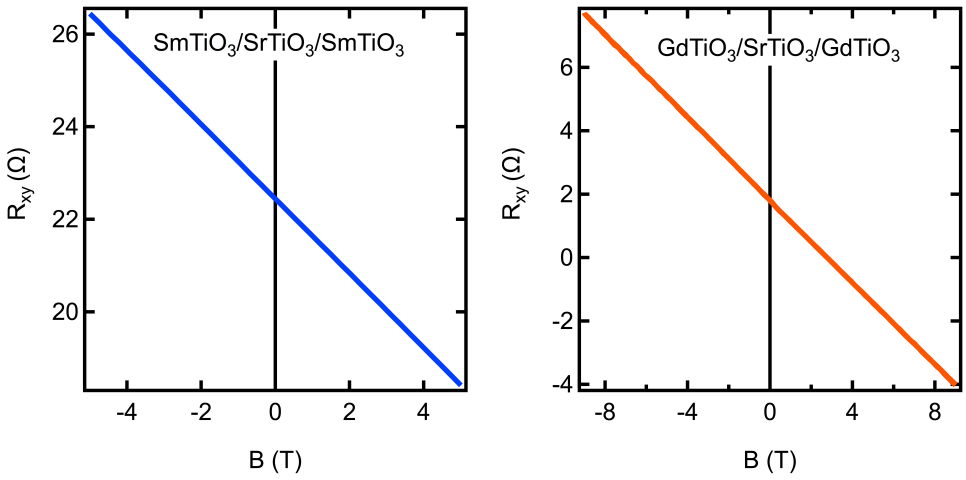

Figure 4.6: Hall resistance R_{xy} with $\beta = 90°$ for both $GdTiO_3$ and $SmTiO_3$ based structures described in the text. Reprinted with permission from **Clayton A. Jackson** and Susanne Stemmer, Physical Review B **88**, 180403(R) (2013), copyright 2013 by the American Physical Society (Ref [2]).

Chapter 5

Quantum Criticality in Complex Oxide Heterostructures

5.1 Introduction

Significant interest has developed in two-dimensional systems near a quantum critical point (QCP) because they are believed to promote the emergence of new ordered states, such as high-temperature superconductivity [20, 21]. Spin fluctuations in antiferromagnetic two-dimensional itinerant systems have been discussed as a possible avenue for high-T_c superconductors [108]. The nature of electronic quasipaticles is altered by interactions with quantum critical fluctuations associated with a quantum phase transition, causing phenomena such as non-Fermi liquid behavior [63, 109, 110]. A generic depiction of a phase diagram for a quantum critical system is featured in Figure 5.1, where the x-axis is the control parameter and the y-axis is the temperature. Because of the atomic-layer precision control of their growth, oxide thin film heterostructures offer new ways to test the theoretical understanding of quantum criticality that are not possible with bulk materials. Heterostructures offer the possibility of tuning system dimensionality by changing layer thicknesses and utilizing electrostatic confinement, as well as taking advantage of proximity effects [66], the likes of which were discussed in Chapter 4. Electrostatic doping also acts to reduce effects from disorder scattering, which can confound the underlying physics [111, 112, 113].

Parts of this chapter are reprinted by permission from Macmillan Publishers Ltd: Nature Communications, 5:4258, **Clayton A. Jackson**, Jack Y. Zhang, Christopher R. Freeze and Susanne Stemmer, copyright (2014).

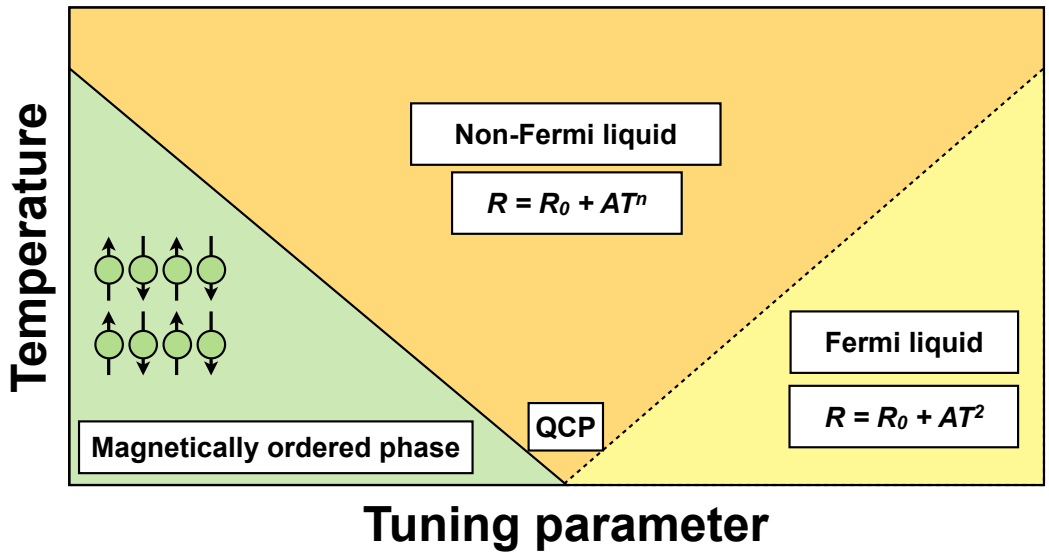

Figure 5.1: Generic phase diagram for systems exhibiting quantum criticality.

In this chapter, we demonstrate non-Fermi liquid behavior in thin $SrTiO_3$ quantum wells embedded in insulating $SmTiO_3$ (an antiferromagnetic Mott insulator with a Néel temperature of $\sim$ 50 K [114]), as a function of temperature, quantum well thickness, and $SmTiO_3$ layer thickness in superlattices. As discussed in Chapters 3 and 4, at sufficiently small quantum well thicknesses, the $SmTiO_3$ insulator that interfaces with the quantum well influences the symmetry of the quantum well and the magnetism of the system, which are intimately linked [5, 2, 4, 115]. We show that the width (which

influences octahedral distortions and effective three-dimensional carrier densities) of the electron system is a tuning parameter for non-Fermi liquid behavior. Compelling evidence for the presence of a quantum critical point and, in the case of the thinnest quantum wells, transition to an itinerant antiferromagnetic phase are presented. Increasing the thickness by a single atomic layer or allowing for interlayer interaction in superlattices both recover Fermi liquid behavior over a wide temperature range. The exponents of the temperature dependence, the symmetry of the order parameter, and the spatial dimensions of the critical fluctuations are discussed and the results are compared with those of quantum wells embedded in ferrimagnetic $GdTiO_3$.

Sample structures

$SmTiO_3/SrTiO_3/SmTiO_3$ structures were grown by hybrid molecular beam epitaxy [81] on (001) LSAT substrates. The quantum well thickness was confirmed by Jack Zhang using scanning transmission electron microscopy. Contacts were deposited by electron beam evaporation using shadow masks for electrical measurements in either Van der Pauw (on as-grown 1×1 cm^2 samples) or Hall bar geometry and consisted of 40 nm Ti/400 nm Au, with the Au being the top layer.

Two types of $SmTiO_3/SrTiO_3/SmTiO_3$ structures were investigated. The first contained single $SrTiO_3$ quantum wells embedded in 20-nm-thick insulating $SmTiO_3$ (10 nm on each side). Throughout this chapter, the thickness of the $SrTiO_3$ quantum wells

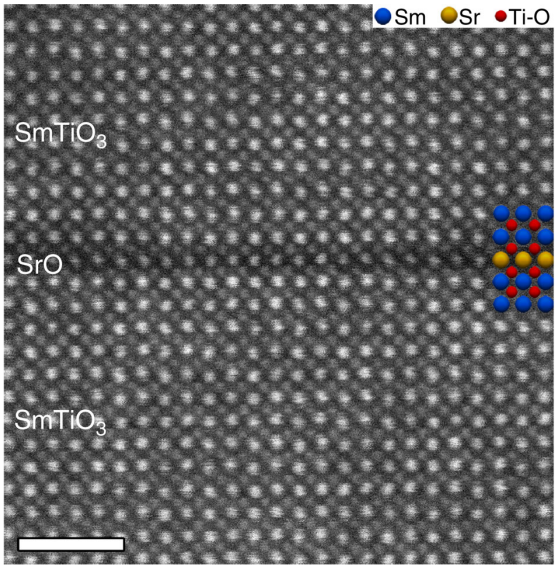

Figure 5.2: Cross-section high-angle annular dark-field scanning transmission electron microscopy image (STEM) of a single SrO layer embedded in $SmTiO_3$, corrected for sample drift. The scale bar is 2 nm. Image taken by Jack Zhang. Reprinted by permission from Macmillan Publishers Ltd: Nature Communications, 5:4258, **Clayton A. Jackson**, Jack Y. Zhang, Christopher R. Freeze and Susanne Stemmer, copyright (2014).

is specified by their number of SrO layers, ranging from 1- and 5-SrO layer(s). The second sample set were superlattices consisting of a single SrO layer in each repeat unit, given by [x $SmTiO_3$/1-SrO]$_y$, where x is the number of pseudocubic $SmTiO_3$ unit cells (u.c.) (the pseudocubic lattice parameter of $SmTiO_3$ is $\sim$ 0.39 nm [43]) and y is the number of repeats. Each superlattice was capped with a $SmTiO_3$ layer with the same thickness as the $SmTiO_3$ in the repeat layer. The $SmTiO_3$ thickness (x) was varied between 1.5 and 16 u.c in the superlattice samples.

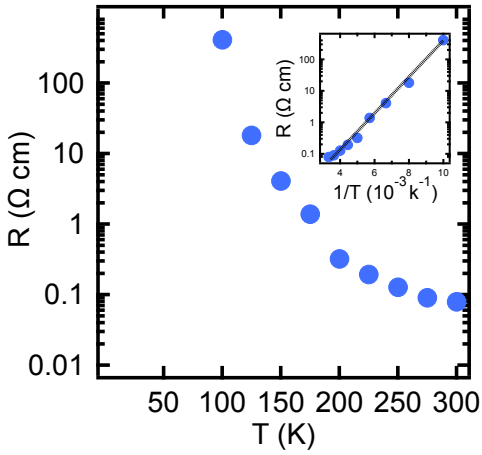

Figure 5.3: Resistivity as a function of temperature for a 10 nm thick $SmTiO_3$ film grown on LSAT. Inset shows same data set vs. 1/T from which an activation energy of 0.11 eV is calculated. Bulk polycrystalline $SmTiO_3$ has an activation energy of 0.15 eV. Reprinted by permission from Macmillan Publishers Ltd: Nature Communications, 5:4258, **Clayton A. Jackson**, Jack Y. Zhang, Christopher R. Freeze and Susanne Stemmer, copyright (2014).

The total sheet resistance of the single quantum well structures has a negligible contribution from the $SmTiO_3$ layers, made evident by Figure 5.3, where the resistivity of a 10 nm thick $SmTiO_3$ film is shown ($\sim$ 0.08 Ω cm at 300 K and $\sim$ 410 Ω cm at 100 K. The measurement apparatus could not obtain a reliable value below 100 K because they were too insulating). All quantum wells, even a single SrO layer, contained $\sim$ 7×10^{14} cm^{-2} mobile carriers (see Figure 5.4). Figure 5.2 shows a representative atomic resolution scanning transmission electron microscopy (STEM) image of a single SrO layer. The thinnest ($<$ 3-SrO layers) quantum wells show symmetry-lowering, orthorhombic-like structural distortions [4].

5.2 Constructing a phase diagram for single quantum well structures

Resistance data were collected using a Physical Property Measurement System (Quantum Design PPMS Dynacool). Samples measured in Hall bar geometry were also measured in Van der Pauw geometry before processing them into Hall bar structures, and the two measurements agreed quantitatively (see Methods chapter). The data shown in Figures 5.5 and 5.10 is from two different 1-SrO quantum well structures, which showed similar transport properties and critical temperature exponents *n*. All fits of the temperature-dependent resistance were performed using a Levenberg-Marquardt non-linear least squares method with IGOR Pro data analysis software. The Tables 5.1 and 5.2 show fitting results obtained for the temperature dependence of the sheet resistance R_s for the $SmTiO_3$/$SrTiO_3$/$SmTiO_3$ single-quantum wells (Table 1) and superlattices (Table 2). The standard deviation for each fit parameter is shown, as well as the R^2 values for the linear fits shown in Figures 5.5 and 5.7, which use the *n* values stated in the Tables.

The sheet resistance R_s as a function of T_n for the single-quantum well samples with different quantum well thicknesses is shown in Figure 5.5, where *T* is the temperature. Fitting was made to equations of form $R_s = R_0 + AT^n$, from which the exponent n was determined. R_0, A and n are fit parameters (see Methods chapter). R_0 is the residual

No. of layers	T range (K)	R_0 (Ω/square)	A (Ω/square K^{-n})	n	R^2 for T^n fit	Data points
1	26-300	1776±17	0.404±0.054	1.586±0.023	0.999186 (n=5/3)	91
2	17-116	392.7±1.3	0.0136±0.0028	2.003±0.043	0.999593 (n=2)	33
2	116-300	353.7±0.8	0.107±0.001	1.607±0.002	0.999952 (n=5/3)	61
3	17-153	366.3±1.2	0.00831±0.00141	2.045±0.034	0.999561 (n=2)	45
3	153-300	335.9±1.2	0.0549±0.0012	1.692±0.004	0.999994 (n=5/3)	49
4	17-168	333.6±1.4	0.0102±0.0017	2.004±0.032	0.999608 (n=2)	50
4	168-300	279.6±0.4	0.110±0.001	1.571±0.001	0.999950 (n=5/3)	44
5	7-191	207.8±1.9	0.0102±0.0027	2.000±0.051	0.999418 (n=2)	41
5	191-300	151.0±0.5	0.0801±0.0006	1.633±0.001	0.999996 (n=5/3)	18

Table 5.1: Fit results for single-quantum well structures with different thicknesses in different temperature ranges. Reprinted by permission from Macmillan Publishers Ltd: Nature Communications, 5:4258, **Clayton A. Jackson**, Jack Y. Zhang, Christopher R. Freeze and Susanne Stemmer, copyright (2014).

No. of unit cells	T range (K)	R_0 (Ω/square)	A (Ω/square K^{-n})	n	R^2 for T^n fit	Data points
1.5	11-159	3.468±0.005	1.09e-4±7e-6	1.993±0.012	0.99994 (n=2)	49
5	23-141	8.16±0.02	2.14e-4±3.0e-5	1.999±0.028	0.99981 (n=2)	39
8	26-135	13.09±0.05	3.34e-4±7.4e-5	2.008±0.045	0.99958 (n=2)	36
12	26-135	31.5±0.2	7.42e-4±2.26e-4	2.013±0.061	0.99921 (n=2)	36
16	59-300	179±4	0.252±0.058	1.222±0.039	0.99900 (n=1.2)	80
16	41-168	190±4	0.138±0.036	1.321±0.044	0.99829 (n=4/3)	86

Table 5.2: Fit results for superlattice structures with different $SmTiO_3$ spacer layer thickness in different temperature ranges. Reprinted by permission from Macmillan Publishers Ltd: Nature Communications, 5:4258, **Clayton A. Jackson**, Jack Y. Zhang, Christopher R. Freeze and Susanne Stemmer, copyright (2014).

sheet resistance and A is the temperature coefficient. The lines in Figure 5.5 are for fixed n values of 2 and 5/3, respectively. The standard deviation for the fits with n as a parameter and the coefficients of determination (R^2 values) for the fits with fixed n are a testament to the quality of fit (see Tables 5.1 and 5.2). Figure 5.5a shows that all quantum wells except the 1-SrO layer follow a T^2 (Fermi liquid) behavior below a transition temperature (given in the labels). Above the transition temperature, the exponent in the temperature dependence changes to n = 5/3 (Figure 5.5b). R_s of the 1-SrO layer follows a $T^{5/3}$ dependence with no transition, as shown in Figure 5.5b. All R_s show an upturn at low temperatures that will be discussed in more detail later in this chapter. Data were only fitted above the R_s minimum. Non-Fermi liquid behavior is indicative of an electron system that is near a QCP [110].

A phase diagram is featured in Figure 5.6 where the circles show the transition temperatures between Fermi liquid and non-Fermi liquid regimes. The x-axis (tuning parameter) is the number of SrO layers in the quantum wells. The 1-SrO quantum well shows non-Fermi liquid behavior over a broad temperature range, consistent with quantum fluctuations that persevere to high temperatures. As can also be seen from Figure 5.5 and Table 5.1 the transition temperature monotonically decreases with decreasing quantum well thickness from $\sim$ 190 K (5-SrO layers) to $\sim$ 120 K (2-SrO layers) to no transition above the temperature of the resistance upturn for the 1-SrO layer quantum well. Thus, analogous to the pressure, magnetic fields, or doping used in bulk, the

width of the quantum well is the tuning parameter for non-Fermi liquid behavior. This phase diagram has characteristics similar to other systems that exhibit quantum critical behavior, in which a larger region of the phase diagram is controlled by the QCP with decreasing temperature.

Superlattices

Figure 5.7 shows results from the superlattices. Previous work in the $GdTiO_3$ system implies that reducing the thickness of $SmTiO_3$ should result in a suppression of octahedral rotations [74]. Since the octahedral tilts of the $SmTiO_3$ influence the degree of tilt in the quantum well [4, 3], it stands to reason that the structure and transport are correspondingly modified. As can be seen from Figure 5.7, the sheet resistance scales monotonically with the thickness of the $SmTiO_3$ layers. As discussed in Chapter 3, magnetism is gradually suppressed in thinner layers, as was previously shown for thin ($<$ 3.5 nm) ferrimagnetic $GdTiO_3$ layers [3]. It is apparent from Figure 5.7 that all superlattices display Fermi liquid behavior over a broad temperature range with the exception of the one with 16 u.c. $SmTiO_3$ ($\sim$ 6.2 nm thickness). R_s of the superlattice with 16 u.c. $SmTiO_3$ layers follows a $T^{4/3}$ dependence (high-quality fits to n of $\sim$ 1.2 were also obtained, excluding the points near the resistance minimum). The superlattice data indicate that disorder is not the origin of the non-Fermi liquid behavior, since the same amount of disorder (that is, interface roughness or point defects) should be

No. of SrO layers	R_0 (Ω/square)	A (Ω/square K^{-n})	n	R^2 for T^n fit
3	1049.7±8.19	0.020507±0.00634	2.0529±0.0584	0.999586 (n=2)
4	379.67±2.09	0.021129±0.00329	1.8987±0.0293	0.999702 (n=2)
5	415.34±2.56	0.011095±0.00236	2.0155±0.0401	0.99964 (n=2)
7	171.33±1.46	0.011358±0.00182	1.9881±0.0305	0.999744 (n=2)

Table 5.3: Fitting parameters for $GdTiO_3$/$SrTiO_3$/$GdTiO_3$. All fits were of the form $R_0 + AT^n$. Reprinted by permission from Macmillan Publishers Ltd: Nature Communications, 5:4258, **Clayton A. Jackson**, Jack Y. Zhang, Christopher R. Freeze and Susanne Stemmer, copyright (2014).

present in all samples, regardless of the spacing between the quantum wells. Furthermore, n = 2 for all quantum wells in $GdTiO_3$ [80], as can be seen in Table 5.3, which are grown under comparable conditions and show similar interface roughness [4].

The value of n is a function of the symmetry of the order parameter and the dimensionality of the fluctuations [21]. A value of 5/3 observed for the quantum wells embedded in thick $SmTiO_3$ is expected for an order wavevector Q = (0,0,0) [19]. Thin quantum wells and $SmTiO_3$ both have orthorhombic symmetry, with a u.c. that is doubled along the parent cubic axes [4]. Thus, the order vector is not Q = (1/2,1/2,1/2) as for a simple cubic antiferromagnet, but Q = (0,0,0), when referred to the orthorhombic cell. The superlattice consisting of 1-SrO layers embedded in 16 u.c. $SmTiO_3$ layers shows an n of 4/3, which is the value expected for a 2D system with Q = (0,0) [19]. It appears that narrowing of the $SmTiO_3$ layers reduces the dimensionality of the fluctuations, which determines n, irrespective of the quasiparticle dimensionality. This

disconnect between quasiparticle collective behavior has been observed in bulk materials [116]. Further investigations are needed to confirm the interpretation of the change in the exponent in the superlattices, since the transport properties are clearly modified. For thinner $SmTiO_3$ layers in the superlattices, we speculate that reduced octahedral tilts and/or wave function overlap of the quantum wells drive the system further from the QCP, recovering Fermi liquid behavior.

Reducing the quantum well thickness increases the 3D carrier density, which brings the quantum well into a regime where on-site Coulomb interactions become relevant [80, 115]. The change in 3D carrier density can be as large as an order of magnitude with a thickness change of just a single SrO layer (see Figure 5.9). Reducing the thickness also impacts the octahedral tilts in the quantum well [4, 3]. The change in 3D carrier density is thus accompanied by a change in the symmetry of the quantum well. In particular, STEM studies (courtesy of Jack Zhang) have shown that structural distortions can be detected in the quantum wells with 2-SrO layers [4]. The symmetry change can have a significant impact on the charge per u.c. and Coulombic interactions in the quantum well [115].

In $GdTiO_3/SrTiO_3/GdTiO_3$, we also observe a similar sensitivity to quantum well thickness. An abrupt metal-insulator transition and a change in resistance by several orders of magnitude is induced by changing the thickness by just 1-SrO layer (from 3- to 2-SrO layers) [80, 4, 3, 91]. Quantum wells in $GdTiO_3$ with thicknesses just above

the metal-insulator transition are ferromagnetic (see Chapter 4). Mass enhancement is seen in transport, but they do not deviate from Fermi liquid behavior [80, 2] as can be seen from Figure 5.8 and Table 5.3. The $SmTiO_3$/$SrTiO_3$/$SmTiO_3$ quantum wells show no mass enhancement as can be seen from the A coefficient in Figure 5.9.

In addition, the $SmTiO_3$ based structures are all conducting regardless of thickness, show significantly smaller distortions in the quantum well [4], and compelling evidence for quantum criticality. In general, there is a strong coupling between orbital order, which correlates with the type of magnetic order [43, 37, 71, 72], and the degree of structural distortions. It is possible that the degree of lattice distortion (and thus the orbital order) determines the nature of the magnetic order in the phase diagram. The degree of lattice distortion is a function of the adjacent rare earth titanate (greater in the case of $GdTiO_3$ relative to $SmTiO_3$), quantum well thickness and superlattice spacer layer thickness. In comparing results in Chapters 4 and 5, It is evident that only proximity to an itinerant antiferromagnetic phase results in non-Fermi liquid behavior.

5.3 Magnetoresistance

Figure 5.10 shows the magnetoresistance of a 1-SrO single-quantum well sample. The magnetic field **B** is in the plane of the film and the current is orthogonal to **B**. Below $\sim$ 20 K, the magnetoresistance changes sign from weakly positive to negative.

At low fields and temperatures ($\sim$ 4 K), the magnetoresistance changes again. At 2 K, the magnetoresistance is positive up to a critical field, $\mathbf{B}_c$ ($\sim$ 2.5 T), then becomes negative for $\mathbf{B} > \mathbf{B}_c$. As shown in Figure 5.11 the positive magnetoresistance at low fields becomes very weak as the thickness of the quantum well is increased by just 1-SrO layer and vanishes for thicker quantum wells.

Positive magnetoresistance can occur in antiferromagnets from the moments aligning antiparallel to **B** [117], and in spin density wave (SDW) systems from suppression of the SDW by the magnetic field, leading to enhanced spin scattering. Positive magnetoresistance has been observed in many SDW systems [118, 119, 120]. This suggests that the QCP is located in the viscinity between the 1- and 2-SrO layer quantum wells, as indicated in Figure 5.6. In Chapter 7, a method of further study is suggested to ascertain the presence and type of magnetic order in the 1-SrO layers.

As illustrated in Figures 5.10 and 5.11 at low temperatures, all samples show an increase in resistance, which was also seen in quantum wells in $GdTiO_3$ [2]. The temperature of the upturn is indicated by the dotted line in Figure 5.6. For all quantum wells, a significant portion of the high-density electron system is located within the first few TiO_2 layers near the interface with the insulating magnet [121, 101]. The upturn in resistance could be attributed to scattering from those moments as they align with lower temperature. The upturn in the resistance is less pronounced for thicker quantum wells, possibly due to a larger spread of the electron gas further away from

the interface. This is a separate effect that does not affect the main conclusions of this chapter. Weak localization can also produce a negative magnetoresistance in 2D systems [122] and has been observed in $SrTiO_3$ [98, 123, 124, 125], but it only appears as a correction to the resistances close to strong localization ($R_s \sim 25$ K Ω/square).

5.4 Chapter summary

In summary, we have shown compelling evidence in electrical transport that two-dimensional, high-density electron systems in oxide heterostructures can exhibit quantum critical behavior. This behavior can be tuned by altering the quantum well width and spacing between quantum wells, which influences both the effective three-dimensional carrier density, symmetry and interaction between neighboring quantum wells. These heterostructures create opportunity for exploration of non-Fermi liquid behavior. Analogous to bulk quantum critical materials, other tuning parameters may give access to nearby QCPs, such as strain or growth on different substrate orientations.

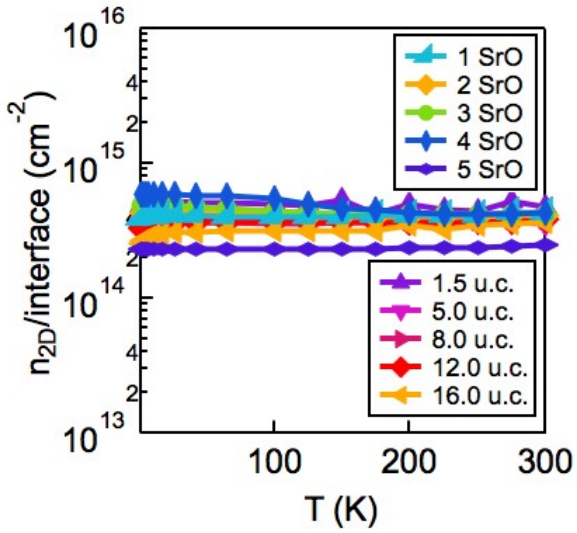

Figure 5.4: Hall sheet carrier densities *per interface* for superlattices and single quantum wells. The thickness of the $SmTiO_3$ layer in the superlattice structure is specified in unit cells (u.c.) while the width of the quantum wells is specified by the number of SrO layers. The carrier densities are calculated assuming a single carrier type where $n_{2D} = 1/(eR_H)$. At room temperature, carriers at different distances from the interface have approximately the same mobility limited by phonon scattering. Thus, it is reasonable to assume the single carrier model yields an accurate estimate of the real carrier density. At lower temperatures, carriers in different subbands with differing proximity to the interface will have various mobilities, leading to apparent changes in the effective 2D density. Reprinted by permission from Macmillan Publishers Ltd: Nature Communications, 5:4258, **Clayton A. Jackson**, Jack Y. Zhang, Christopher R. Freeze and Susanne Stemmer, copyright (2014).

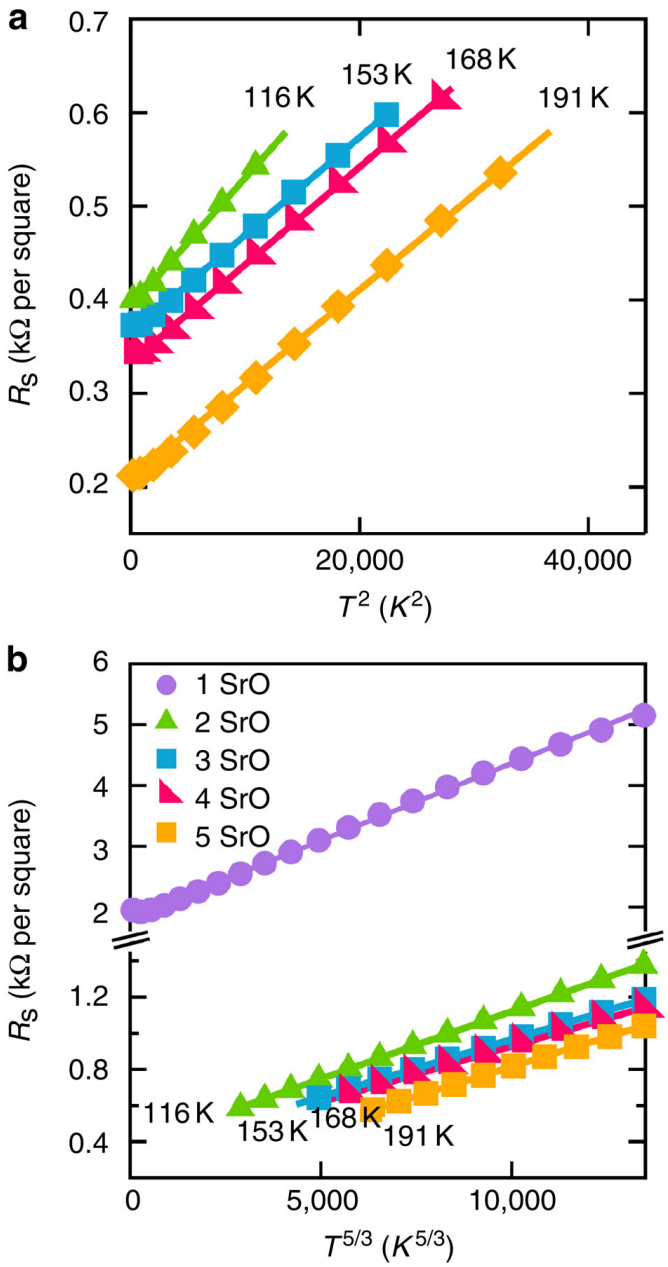

Figure 5.5: **a)** R_s on a T^2 scale below the transition temperature to non-Fermi liquid behavior. Linear fits are of the form $R_0 + AT^2$. **b)** R_s above the transition temperature plotted on a $T^{5/3}$ scale. Linear fits are of the form $R_0 + AT^{5/3}$. Reprinted by permission from Macmillan Publishers Ltd: Nature Communications, 5:4258, **Clayton A. Jackson**, Jack Y. Zhang, Christopher R. Freeze and Susanne Stemmer, copyright (2014).

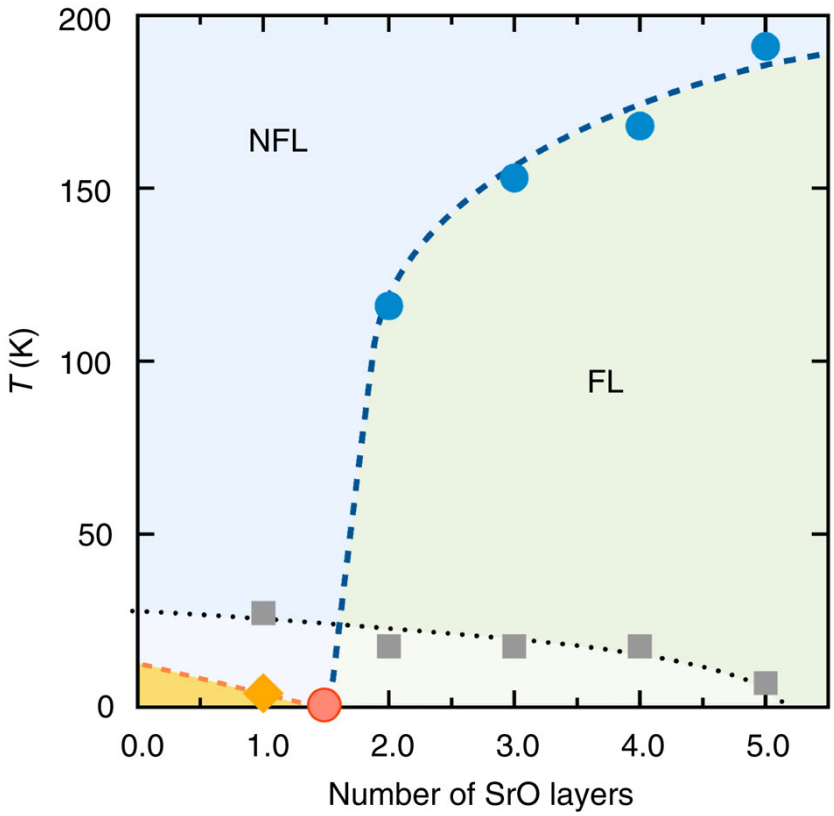

Figure 5.6: Phase diagram showing Fermi/non-Fermi liquid behavior vs quantum well width. Reprinted by permission from Macmillan Publishers Ltd: Nature Communications, 5:4258, **Clayton A. Jackson**, Jack Y. Zhang, Christopher R. Freeze and Susanne Stemmer, copyright (2014).

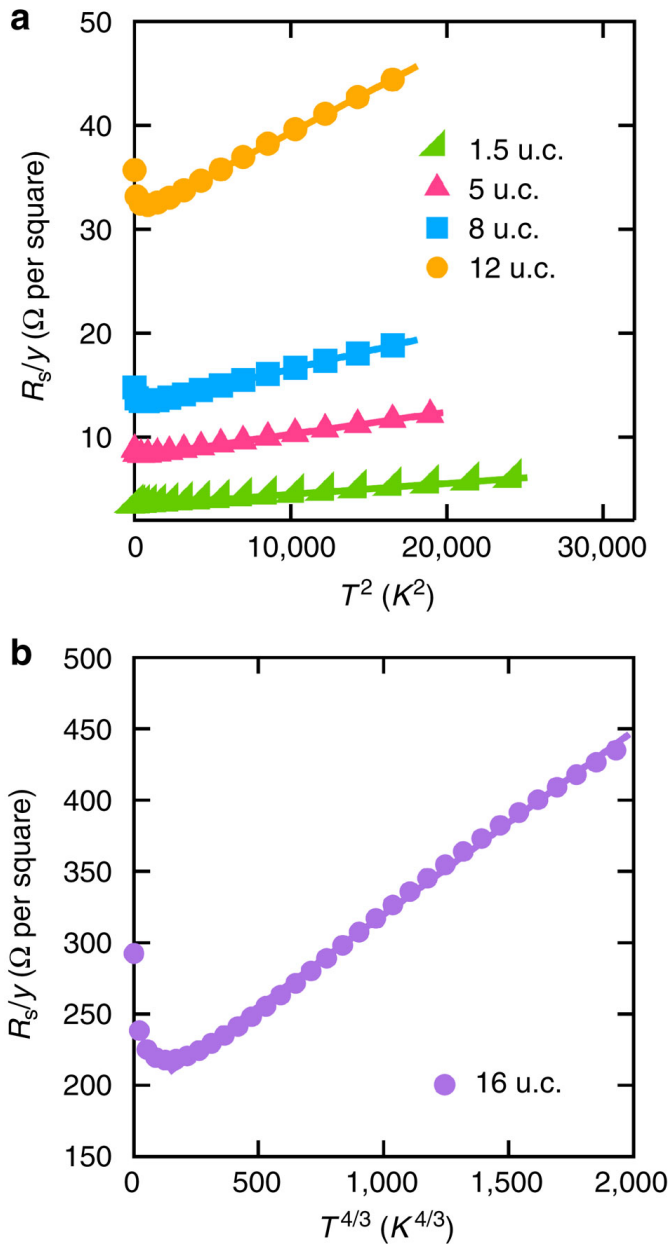

Figure 5.7: a) R_s as a function of T^2 for superlattice structures composed of single SrO layers separated by different $SmTiO_3$ layer thicknesses, specified in unit cells. Linear fits are of the form $R_0 + AT^2$. The number of repeats are 14 for 1.5, 5 and 8 u.c. and 8 for 12 u.c.. **b)** R_s vs $T^{4/3}$ for the 16 u.c. structure. The linear fit is of the form $R_0 + AT^{4/3}$. The number of repeats is 6. The sheet resistance is given per SrO layer for all structures. Reprinted by permission from Macmillan Publishers Ltd: Nature Communications, 5:4258, **Clayton A. Jackson**, Jack Y. Zhang, Christopher R. Freeze and Susanne Stemmer, copyright (2014).

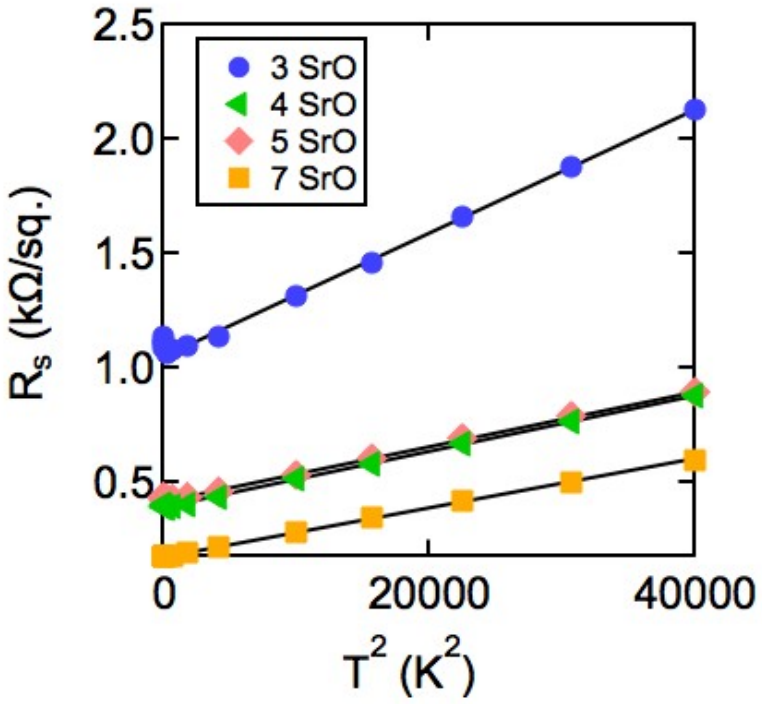

Figure 5.8: R_s as a function of T^2 for a sample series of $GdTiO_3/SrTiO_3/GdTiO_3$ quantum wells with different $SrTiO_3$ layer thickness, given in number of SrO layers. The lines are a fit of the form $R_0 + AT^2$. Reprinted by permission from Macmillan Publishers Ltd: Nature Communications, 5:4258, **Clayton A. Jackson**, Jack Y. Zhang, Christopher R. Freeze and Susanne Stemmer, copyright (2014).

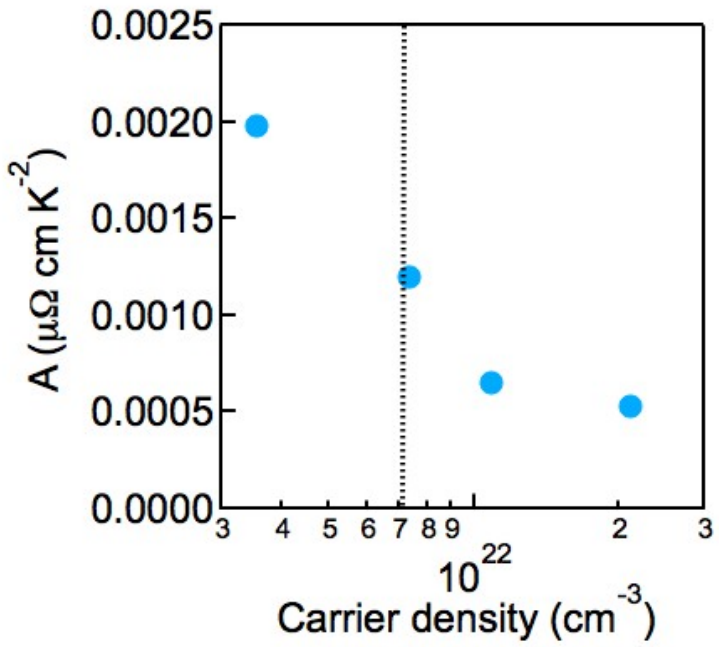

Figure 5.9: Temperature coefficient A in the Fermi liquid regime vs. 3D carrier density in the single quantum well structures. The 3D density is calculated by dividing the room temperature 2D Hall density by the width of the quantum well. A continuous decrease is expected if there is no mass enhancement. Reprinted by permission from Macmillan Publishers Ltd: Nature Communications, 5:4258, **Clayton A. Jackson**, Jack Y. Zhang, Christopher R. Freeze and Susanne Stemmer, copyright (2014).

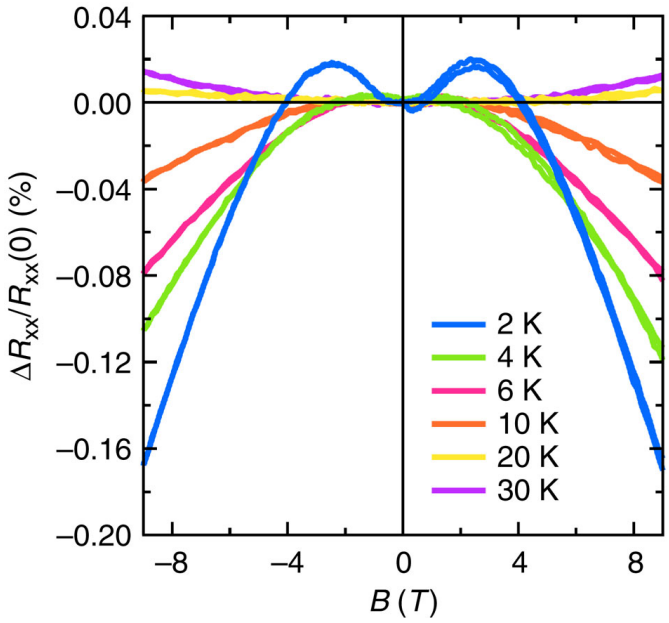

Figure 5.10: Temperature dependence of the magnetoresistance for a single SrO layer embedded in $SmTiO_3$. The magnetic field was swept from +9 to -9 and back to +9 T. Reprinted by permission from Macmillan Publishers Ltd: Nature Communications, 5:4258, **Clayton A. Jackson**, Jack Y. Zhang, Christopher R. Freeze and Susanne Stemmer, copyright (2014).

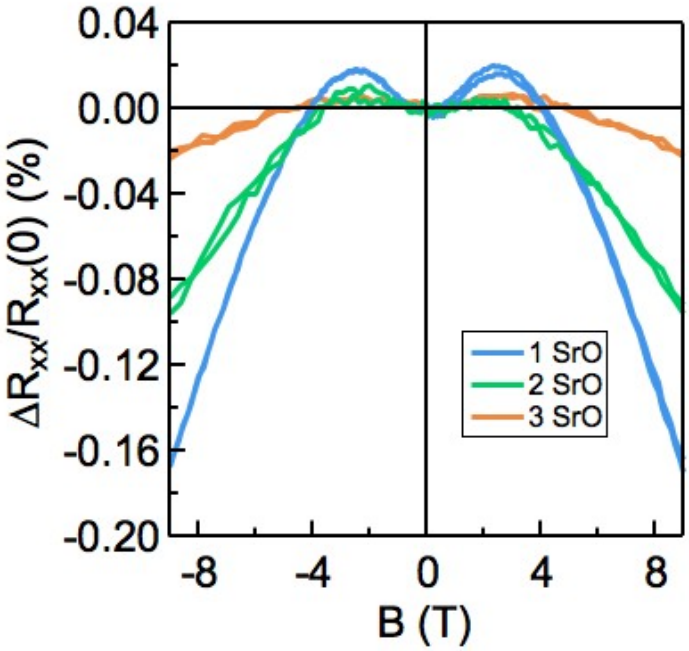

Figure 5.11: Relative magnetoresistance for 1, 2 and 3 SrO thick quantum wells. For all measurements, B was swept from +9 to -9 and back to +9 T. The magnetic field was in the plane of the film and orthogonal to the current. reprinted by permission from Macmillan Publishers Ltd: Nature Communications, 5:4258, **Clayton A. Jackson**, Jack Y. Zhang, Christopher R. Freeze and Susanne Stemmer, copyright (2014).

Chapter 6

Devices

6.1 Introduction

In this chapter, we focus on *application* driven experiments in the $SrTiO_3$/$GdTiO_3$ system. In particular, emphasis is placed on utilizing the high density 2DEG at the interface for transistor device applications, relevant in fields such as power conditioning, microwave communications and radar electronics [126]. This Chapter begins with work in capacitance-voltage analysis, in which a one-dimensional, resistive transmission line model is used to determine C-V characteristics from the frequency dependent admittance. The results yield an estimate for the field dependent dielectric constant of the $SrTiO_3$ layer, the degree of modulation of the 2DEG by the maximum applied voltage, and an upper limit of the unintentional dopant density in the $SrTiO_3$. The chapter closes with a brief review of collaborative work in developing a high-performance field effect transistor in the $SrTiO_3$/$GdTiO_3$ system.

6.2 Capacitance-Voltage Analysis

Characterizing the spatial extent of the charge carriers at the Mott/band Interface [127, 128, 81, 12] is of great importance to understand the nature of the 2DEG in this system. Additional carriers may be present as a result of the reducing growth

Parts of this chapter are reprinted with permission from Appl. Phys. Lett. 100, 232106 (2012), by **Clayton A. Jackson**, Pouya Moetakef, S. James Allen and Susanne Stemmer.

conditions (see chapter on methods). In addition, gating control of these high charge carrier densities is the first step in realizing field-effect devices [129]. In capacitance-voltage (C-V) profiling, the depletion width, t, of a reverse-biased Schottky barrier is changed by an applied voltage. This is a well-established method for characterizing the carrier density distribution of semiconductor heterojunctions [130]. To determine the depletion width from the admittance, the series resistance [131] must be accounted for. In this section, we report on applying C-V analysis to $SrTiO_3$/$GdTiO_3$ interfaces.

$SrTiO_3$/$GdTiO_3$ heterostructures were grown on (001) LSAT single crystals by hybrid MBE as described in detail elsewhere (See Methods Chapter and [81, 132]). The $SrTiO_3$ and $GdTiO_3$ layers were 40 nm and 8 nm thick, respectively. Coplanar C-V structures were fabricated by e-beam evaporation of 50-nm-thick Au Schottky gate contacts and Ohmic Al/Ni/Au contacts of thickness 50/20/150 nm (see Figure 6.1a). Each of the three contacts measured 130 μm $\times$ 150 μm and their separation was 50 μm. I-V characteristics were measured at 300 K and 221 K using a HP 4155B semiconductor parameter analyzer (Hewlett Packard, Palo Alto, CA) and cryogenic wafer probe station (MMR technologies, Mountain View, Ca). The source-drain (Ohmic) and source-gate (Schottky) current-voltage (I-V) characteristics are shown in Figure 6.1 b and c. The I-V curves show a decrease in leakage with temperature, and are nearly symmetric with respect to the applied gate bias. An impedance analyzer (Agilent model 4294A, Palo Alto, CA) was used to measure the complex impedance and admittance as a function

of frequency (40 Hz - 100 MHz) at different DC bias voltages applied to the gate. Both forward and reverse bias measurements were made on multiple devices. The amplitude of the AC signal was 100 mV for all measurements. To further minimize thermionic emission across the Schottky barrier, measurements were carried out at $\sim$ 130 K using a cryogenic wafer probe station (RMC Cryosystems, Tucson, AZ) . The temperatures at which impedance and I-V characteristics were measured were set by the lower limits of the apparatus used.

A one-dimensional transmission line model was used to quantify gate conductance, capacitive and dielectric loss for a wide range of applied biases and measurement frequencies. Using this model, C-V characteristics could be determined from the frequency dependent admittance. In this model, the complex admittance beneath the gate is given by:

$$Y_{gate} = \frac{2l}{kt}(\sigma + i\omega\epsilon_0\epsilon_r)\tanh(\frac{kw}{2}) \tag{6.1}$$

where l and w are the dimensions of the gate, σ the conductivity of the gate due to leakage, ω is the radial frequency, ϵ_0 the permattivity of free space, ϵ_r the dielectric constant and k is given by:

$$k = \sqrt{(\frac{\rho}{t}(\sigma + i\omega\epsilon_0\epsilon_r))} \tag{6.2}$$

where ρ is the sheet resistance. The total device admittance is given by:

$$Y_{total} = (\frac{\rho}{3} + \frac{1}{Y_{gate}})^{-1} \tag{6.3}$$

where the ρ/3 term is a geometry-dependent series resistance accounting for all resistive elements between the source and gate, including contact resistance. The prefactor of 1/3 was obtained from fitting of the data. The fitting of the device admittance as a function of frequency was done using σ/t, ρ and ϵ_r/t as fit parameters. Prior to device fabrication, the as-grown structure's sheet resistivity vs temperature was measured in Van der Pauw geometry [81, 132], and ρ (Figure 6.2a) was in close agreement with these measurements. This implies a negligible contribution to the series resistance from contact resistance, an indicates the processing steps were not invasive to the transport properties of the films. The fitted conductivity under reverse bias (Figure 6.2b) shows a significant increase at -0.2V, and was consistent with the resistance estimated from the source-gate I-V curve, assuming a fully depleted $SrTiO_3$ layer of 40 nm.

Figure 6.2c shows the C-V characteristics determined from the ϵ_r/t fit parameter, where $C = (\epsilon_0\epsilon_r/t)A$. The capacitance changes by less than 2 mF/m^2 between 0 and - 0.5 V, indicating that the depletion width does not change with bias, and that the high density 2DEG cannot be significantly modulated by the applied gate bias under these conditions. For a 40 nm-thick fully depleted $SrTiO_3$ layer, an upper limit for the dielectric constant of the $SrTiO_3$ of approximately $\epsilon_r \sim 125$ can be established, which is

much lower than the dielectric constant of bulk $SrTiO_3$ at 130 K ($\sim$ 1000 [133, 134]). The dielectric constant of $SrTiO_3$ is sensitive to applied bias [135], strain [23] and possibly oxygen deficiency. The $SrTiO_3$ films in this study were all coherently strained to the LSAT substrate [81] and are therefore under compressive strain, which should increase the out-of-plane dielectric permittivity [23]. For a Schottky barrier height of 1 eV [136], the field, **E**, across the $SrTiO_3$ layer is 2.5 $\times$ 10^7 V/m. At this field, the tunability, n of $SrTiO_3$ is estimated to be $\sim$ 11, where $n = \epsilon_r(0)/\epsilon_r(E)$ and $\epsilon_r(0)$ is the dielectric constant at zero field [135]. This is more than sufficient to account for the suppressed dielectric constant. In addition, local electric fields generated by the high-density 2DEG at the $SrTiO_3$/$GdTIO_3$ interface are an order of magnitude larger ($\sim$ $(qn_{2DEG})/(\epsilon_r\epsilon_0)$, where q is the electron charge), acting to further suppress the dielectric constant at the interface. This also results in a nonuniform permattivity.

The fraction of the 2DEG charge carrier density, n_{2DEG}, that can be modulated is given by:

$$n_{2DEG} = \frac{\epsilon_0\epsilon_r V}{qt}. \tag{6.4}$$

For an applied bias of V = - 0.5V and with ϵ_r = 125, n_{2DEG} is $\sim$ 8.6 $\times$ 10^{12} cm^{-2}, $\sim$ 2.5% of the 2DEG sheet carrier density.

The results can also be used to estimate the unintentional dopant density resulting from the oxygen difficient growth conditions in the $SrTiO_3$. The depletion width of a Schottky barrier is given by:

$$t = \sqrt{\frac{2\epsilon_0\epsilon_r\phi}{qN_d}} \tag{6.5}$$

where ϕ is the barrier height and N_d the dopant density. For a barrier height of 1 eV [136] and $\epsilon_r = 125$, the upper limit for N_d is $\sim 8.6 \times 10^{18}$ cm^{-3}. The low carrier density in the bulk of $SrTiO_3$, compared to the 2DEG density of $\sim 3 \times 10^{14}$ cm^{-2} explains why $SrTiO_3$/$GdTiO_3$ heterostructures and superlattices show no thickness dependence of the sheet carrier density for $SrTiO_3$ thicknesses up to 200 nm [81, 103].

6.3 $SrTiO_3$/$GdTiO_3$ field effect transistors

Oxide materials provide many advantages in field effect transistor performance relative to more traditional semiconductor materials; The high charge density of $\sim 3 \times 10^{14}$ cm^{-2} is an order of magnitude larger than achievable 2DEG densities in semiconductors [126, 137], ideal for high power applications. In addition, the large dielectric constants of oxides allow for greater charge modulation, as evident by equation 6.4, where the charge modulated n_{2DEG} is directly proportional to the dielectric constant ϵ_r.

It is evident from the previous work in C-V analysis that one of the greater challenges in this materials system is the modulation of high charge carrier densities. Recent work has made significant progress toward this goal [137, 138]. In these studies, an "inverted" structure is adopted, consisting of LSAT/$GdTiO_3$/$SrTiO_3$. The inverted structure is advantageous in that it places the gate on the higher dielectric constant material, $SrTiO_3$. It also allows for a reduced gate-channel distance, increasing the intrinsic gate-source capacitance and transconductance relative to any parasitic capacitance, enhancing gain. Initial work showed that an O_2 plasma exposure prior to the gate deposition dramatically improved the rectifying behavior of the gate [137]. However, these studies were limited to a total modulation of $\sim 20\%$.

Further study has revealed the presence of interfacial layers with lower capacitances, lowering the effective capacitance of the entire layer. Counterintuitively, by *increasing* the thickness of the $SrTiO_3$ layer, the effect of the interfacial layer can be reduced, yielding a higher total effective capacitance and higher charge modulation. With this approach, collaborators have effectively modulated over 10^{14} cm^{-2} electrons, the highest charge modulation ever reported [138].

6.4 Chapter summary

In summary, we have shown that C-V analysis of high-density 2DEGs at Mott/band insulator interfaces requires accounting for the conductance and sheet resistance of the structures and allows for determining the dielectric constant of the $SrTiO_3$ layer and estimates of the bulk dopant density. These results provide for an estimate of the degree to which interfacial charge carriers at the interface can be modulated by an applied gate voltage. In addition, we have shown that improved processing techniques and structural design can dramatically improve the transistor performance of $SrTiO_3$/$GdTiO_3$ based heterostructure devices.

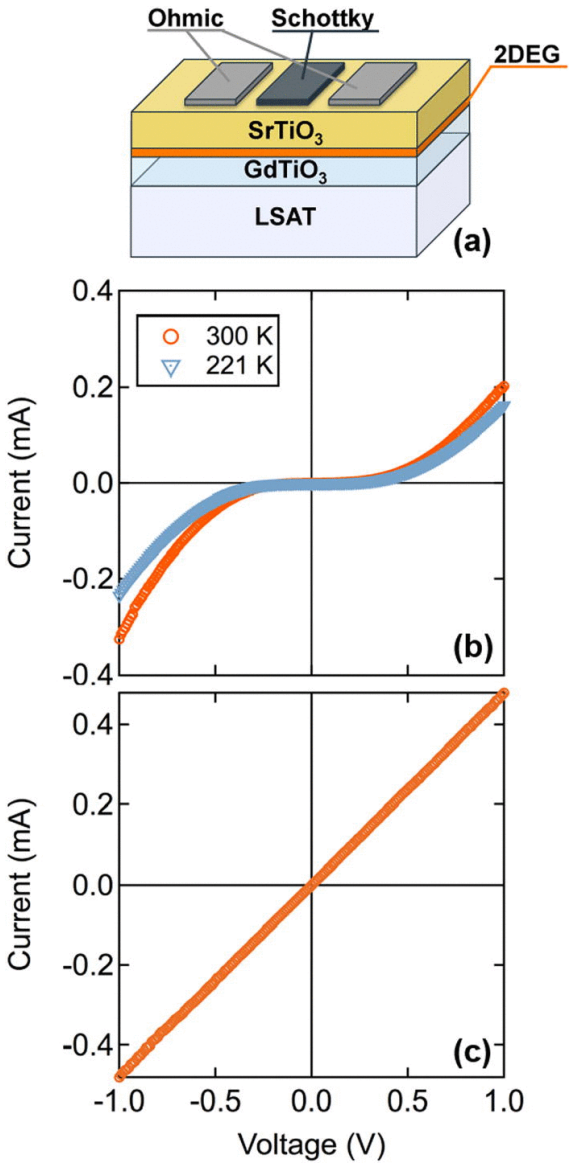

Figure 6.1: **(a)** Device structure. **(b)** Source-Gate I-V characteristics at room temperature and at 221 K. **(c)** Source-drain I-V characteristics at room temperature. Reprinted with permission from Appl. Phys. Lett. 100, 232106 (2012), by **Clayton A. Jackson**, Pouya Moetakef, S. James Allen and Susanne Stemmer. Copyright (2012), AIP Publishing LLC.

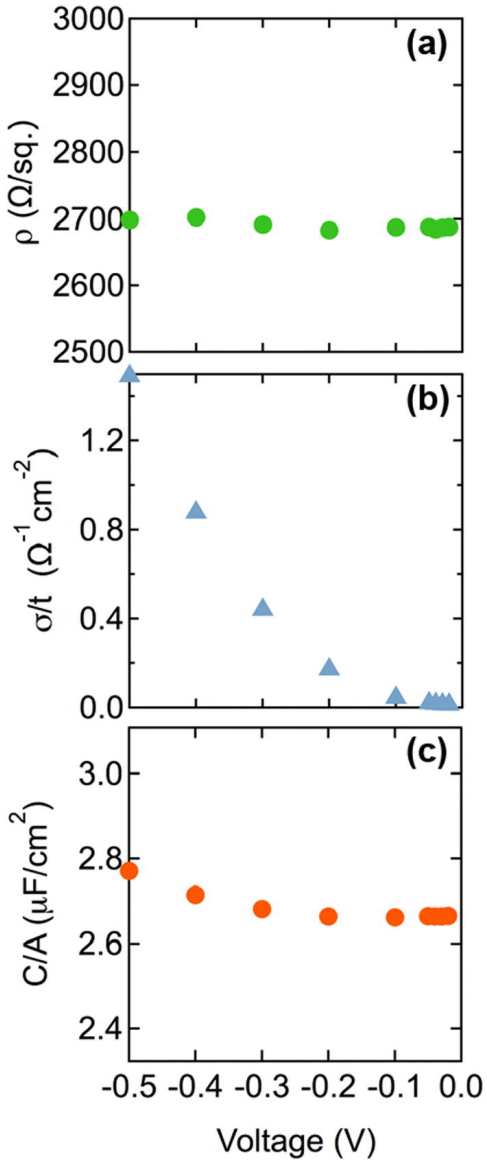

Figure 6.2: **(a)** Sheet resistance ρ as a function of voltage applied to the schottky gate. **(b)** Fit parameter ρ/t vs. voltage. **(c)** C-V characteristics extracted from the fit parameter ϵ_r/t. Reprinted with permission from Appl. Phys. Lett. 100, 232106 (2012), by **Clayton A. Jackson**, Pouya Moetakef, S. James Allen and Susanne Stemmer. Copyright (2012), AIP Publishing LLC.

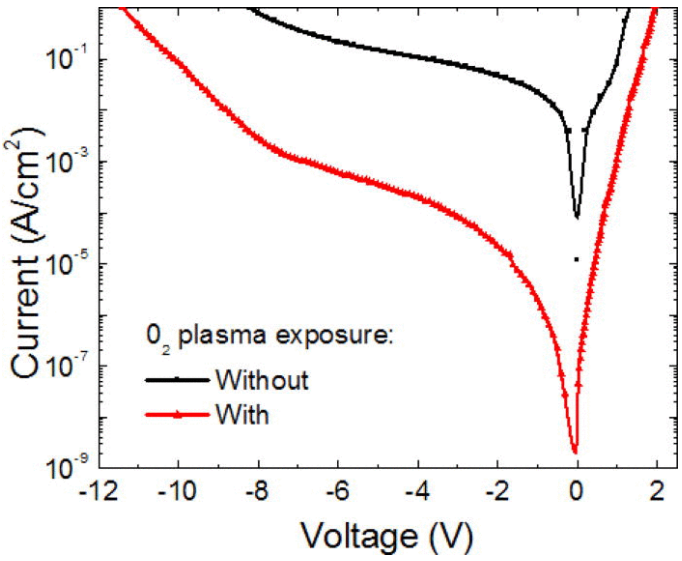

Figure 6.3: I-V characteristics of Schottky contacts with and without a 30 minute O_2 exposure. Reprinted with permission from Appl. Phys. Lett. 102, 242909 (2013), by M. Boucherit, O. F. Shoron, T. A. Cain, C. Jackson, S. Stemmer, and S. Rajan, Copyright (2013), AIP Publishing LLC.

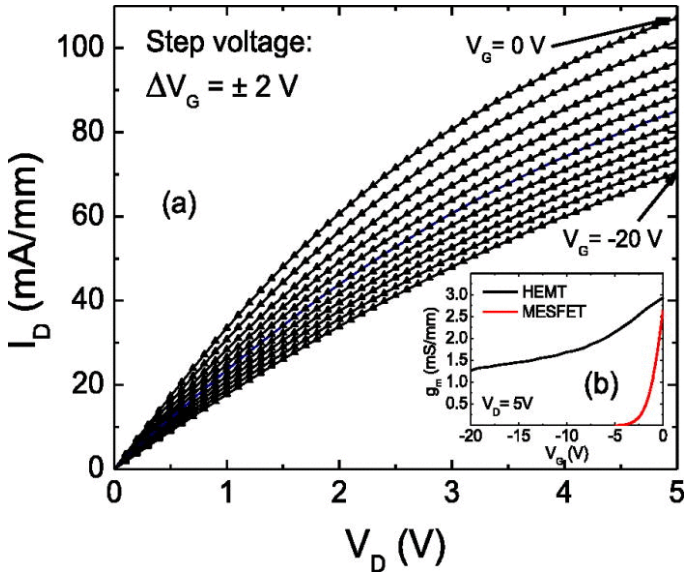

Figure 6.4: **(a)** Measured output characteristics for $SrTiO_3/GdTiO_3$ heterostructure field-effects transistor. **(b)** Transconductance profile of the $SrTiO_3/GdTiO_3$ structure (labeled HEMT). Also shown for comparison is a metal-semiconductor field effect transistor (MESFET) consisting only of $SrTiO_3$ for comparison. Reprinted with permission from Appl. Phys. Lett. 104, 182904 (2014) M. Boucherit, O. Shoron, C. A. Jackson, T. A. Cain, M. L. C. Buffon, C. Polchinski, S. Stemmer, and S. Rajan, Copyright (2014), AIP Publishing LLC.

Chapter 7

Summary and Future Works

7.1 Summary

The intent of this dissertation has been to study the relationships between emergent phenomena and heterostructures and to develop controllable states using advanced growth and characterization techniques. The systems studied were Mott/band insulator heterostructures composed of $SmTiO_3$/$SrTiO_3$ and $GdTiO_3$/$SrTiO_3$. The first two Chapters provided the reader with a motivational introduction and overview of materials properties of interest. Hybrid molecular beam epitaxy was discussed as the primary method to produce thin film heterostructures and it was shown that electrical transport characterization methods can be used to characterize the novel structures of interest throughout this work.

In Chapter 3, heterostructures composed of $SrTiO_3$/$SmTiO_3$ and $SrTiO_3$/$GdTiO_3$ were studied in order to better understand the role that strain and octahedral connectivity has on orbital order and the structural Ti-O array as it pertains to magnetism and transport. For thin $GdTiO_3$ layers sandwiched between $SrTiO_3$, it was found that suppression of ferromagnetism is coincident with the thinning of the $GdTiO_3$, and is gone entirely at a thickness of 2.0 nm. The results indicate that the FM ground state is controlled by the narrow bandwidth, exchange and orbital ordering. For $SrTiO_3$ embedded in $SmTiO_3$ and $GdTiO_3$, a decrease in film thickness, which relates to the degree of distortion in the film, corresponds with a metal-insulator transition if the

material in which it is embedded has sufficient distortion, made evident in comparing $SmTiO_3/SrTiO_3/SmTiO_3$ and $GdTiO_3/SrTiO_3/GdTiO_3$ heterostructures.

Prior to this work, emergent magnetic states have been observed in Mott/band heterostructures, but the influence of proximity effects and exchange coupling was not fully resolved. Chapter 4 was dedicated to the investigation of proximity effects in heterostructures using the angular dependence of the magnetoresistance of thin (< 1 nm), metallic $SrTiO_3$ quantum wells epitaxially embedded in $GdTiO_3$ and $SmTiO_3$. It was shown that the longitudinal and transverse magnetoresistance in the structures with $GdTiO_3$ are consistent with anisotropic magnetoresistance, and thus indicative of induced ferromagnetism in the $SrTiO_3$. Comparison with the structures with antiferromagnetic $SmTiO_3$ showed that the properties of thin $SrTiO_3$ quantum wells can be tuned to obtain magnetic states that do not exist in the bulk material.

Another goal of this work was to better understand the effect of magnetically ordered layers on neighboring low-dimensional itinerant systems. Chapter 5 discussed the emergence of novel states with a focus on compelling evidence that two-dimensional, high-density electron systems in oxide heterostructures can exhibit quantum critical behavior. It was shown that the observed behavior was a function of quantum well width and spacing between quantum wells, which influenced both the effective three-dimensional carrier density, symmetry and interaction between neighboring quantum wells.

In Chapter 6, it was shown that C-V analysis of high-density 2DEGs at Mott/band insulator interfaces requires accounting for the conductance and sheet resistance of the structures and allows for determining the dielectric constant of the $SrTiO_3$ layer and estimates of the bulk dopant density. Using C-V analysis, we were able to estimate the degree to which interfacial charge carriers can be modulated by an applied gate voltage. It was also shown that improved processing techniques and heterostructure design can significantly improve the transistor performance of $SrTiO_3$/$GdTiO_3$ based heterostructure devices.

7.2 Future works

As we have seen in previous chapters, heterostructures consisting of narrow $SrTiO_3$ quantum wells show unique emergent phenomena, including extreme interfacial carrier densities and strong evidence for itinerant magnetically ordered states. Thus far, the primary control parameter has been structural change in the system. Two questions that still remain is the relative role of the different components of the system (carrier density, structural distortion, orbital order, etc), and the nature of the magnetically ordered states if present. In this chapter, we discuss potential future works to further elucidate these questions.

To decouple the relative role of the different degrees of freedom in these structures, we need additional methods of *tuning* emergent behavior in heterostructures. We will discuss utilizing the success of charge modulation, featured in Chapter 6, as a method of developing a better understanding of the carrier densities specific part in emergent phenomena.

While many of the measurements featured in this work show strong evidence and present compelling arguments for the presence of magnetism, none give a direct, precise measure of magnetic order. Thus, we will discuss more direct measurement methods that can be employed to elucidate the itinerant magnetically ordered states in the thinnest quantum wells.

7.2.1 Tuning emergent behavior in heterostructures

In Chapter 6, we discussed our collaborator's great success in achieving record high charge modulation in the $SrTiO_3$/$GdTiO_3$ system [137, 138]. In Chapters 4 and 5, we discussed the emergence of ferromagnetic ordered states in thin $GdTiO_3$/$SrTiO_3$/$GdTiO_3$ heterostructures, and compelling evidence for the emergence of an itinerant antiferromagnetic state in very narrow $SmTiO_3$/$SrTiO_3$/$SmTiO_3$ quantum wells. The emergent magnetically ordered state only appears when the quantum wells become sufficiently thin, which effects both the three-dimensional carrier density in the quantum well [2, 45] as well as the degree of structural distortion [74]. One very compelling

future work is to combine the results of Chapters 4, 5 and 6 with the intent of probing the *carrier density's* specific role in the quantum well's behavior. This would allow for a direct measure of the relative role that carrier density plays in these systems. Furthermore, in the event that the emergent phenomena is contingent upon the presence of extreme carrier densities, it would allow for a tunable magnetically ordered state. This could be accomplished both through charge injection into wider quantum wells, and depletion of the most narrow quantum wells.

7.2.2 Polarized neutron reflectivity

As we have seen, proximity effects at interfaces between magnetic insulators and conductors with strong spin-orbit coupling have shown the emergence of novel states that show strong indications of magnetic order in transport [2, 45]. Thin ($<$ 2 nm) quantum wells of $SrTiO_3$ embedded in $GdTiO_3$ show magnetoresistance hysteresis at temperatures below $\sim$ 8 K [81]. In Chapter 4, we discussed angular-dependent magnetoresistance studies of narrow $SrTiO_3$ quantum wells, embedded in ferrimagnetic $GdTiO_3$. The results were consistent with exchange coupling induced ferromagnetism in the $SrTiO_3$. In Chapter 5, we observed positive magnetoresistance in the thinnest $SrTiO_3$ quantum wells embedded in $SmTiO_3$, consistent with the emergence of an itinerant antiferromagnetic state.

Although these observations are consistent with emergent magnetism in the conducting $SrTiO_3$ layers of these structures, the study is lacking in a direct measure of the local magnetic structure of the sample. Measurements such as SQUID (superconducting quantum interference devices) only provide insight into the net magnetization of the entire structure, and cannot exclude the magnetism of the $RTiO_3$ (R = Gd, Sm) or the film substrate. Thus, a method of analysis that can give a magnetic depth profile of the structure is needed to complete our current understanding of the system.

A magnetic depth profile can be obtained by measurement of polarized neutron reflectivity, in which the non-spin-flip neutron reflectivity is measured as a function of transfer wave-vector Q for neutrons spin polarized parallel (ρ^{++}) or anti-parallel (ρ^{--}) to an applied magnetic field. These reflectivities can be calculated and modeled precisely from the depth dependent scattering potentials (scattering length density, SLD) of the sample structure

$$\rho^{++} = \rho_N + CM \tag{7.1}$$

and

$$\rho^{--} = \rho_N - CM \tag{7.2}$$

where ρ_N is the (complex) contribution from the nuclear composition and CM a term directly proportional to the component of the in-plane magnetization (moment per unit volume) parallel to the applied field. By modeling the spin-dependent reflectivity

data, we can determine the depth profiles of the nuclear composition and the in-plane magnetization.

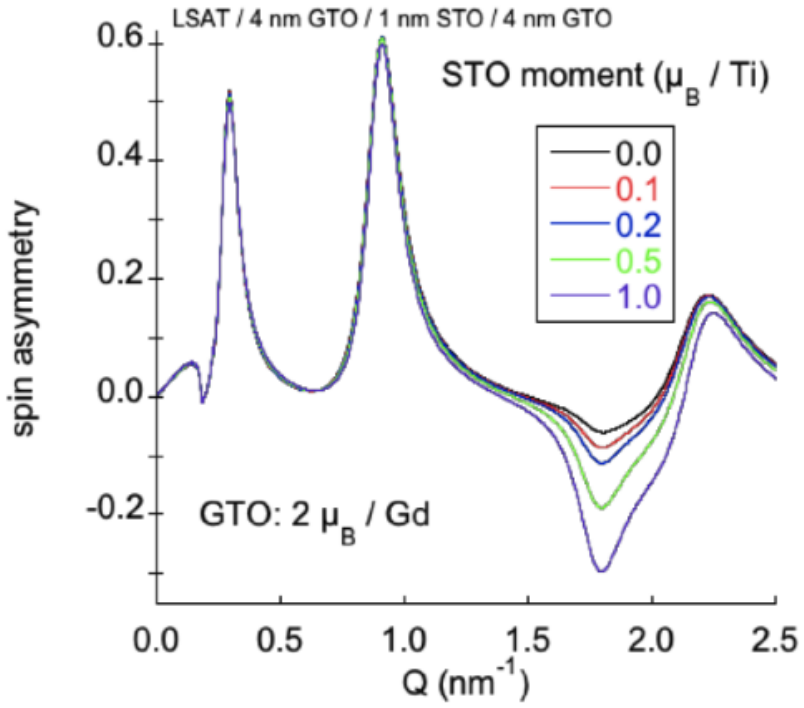

Figure 7.1: Calculated spin asymmetries (the difference between (ρ^{++}) and (ρ^{--}), divided by the sum) for a $\sim$ 2 SrO thick $SrTiO_3$ quantum well embedded in 8 nm of $GdTiO_3$. Calculation courtesy of Brian Kirby.

Figure 7.1 shows the calculated magnetic signal (spin asymmetries) for several values of a single $\sim$ 2 SrO thick $SrTiO_3$ quantum well embedded in $GdTiO_3$ with different possible magnetic moments associated with the $SrTiO_3$. The different signals diverge noticeably near Q = 1.8 nm^{-1}, demonstrating that it is possible to detect a magnetic signal directly from the $SrTiO_3$. Figure 7.2 shows preliminary high temperature (100

K) measurements that gives values of Q across several orders of magnitude. This Q-spectrum is consistent with a high quality sample structure, demonstrating the viability of the intended experiment.

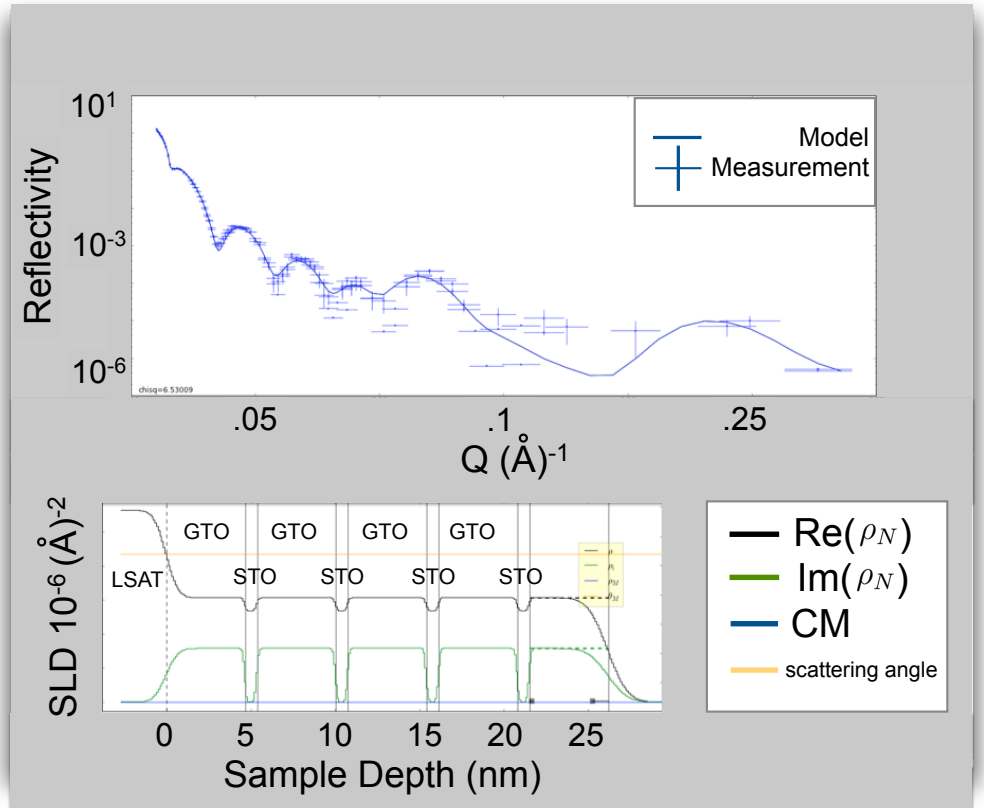

Figure 7.2: Top: Fitted reflectivity (ρ^{++} and ρ^{--}) vs Q data at 100 K for a $GdTiO_3$ / $SrTiO_3$ 5 layer repeat superlattice structure. **Bottom**: Modeled magnetic depth profile components $Re(\rho_N)$, $Im(\rho_N)$, CM and scattering angle. Measurement and modeling courtesy of Brian Kirby.

The onset of the hysteresis (presumably the T_c for the $SrTiO_3$) occurs around 5 - 10 K (See Figure 4.1). Thus, a series of measurements of the non-spin-flip reflectivity at sufficient magnetic fields, with measurements taken at temperatures well above

the T_c of $GdTiO_3$, below the T_c of $GdTiO_3$ and above the onset of magnetoresistance hysteresis, and below the presumed T_c of The $SrTiO_3$, Should elucidate any magnetic moment associated with the $SrTiO_3$. Scans performed on two films, one with thin ($<$ 2 nm) quantum wells of $SrTiO_3$ in which hysteresis is observed, and one with thicker ($>$ 2 nm), could be used to further confirm any moment associated directly with the magnetism of the $SrTiO_3$.

For $SrTiO_3$ embedded in $SmTiO_3$, a different approach may be necessary, due to the thickness of the structure, and the magnetic fields and temperatures needed to observe emergent magnetic order. An alternative to neutron reflectivity is resonant inelastic x-ray scattering, or RIXS, in which high energy photons are scattered off a solid. This method benefits from a considerably stronger interaction than neutron scattering, giving larger signals and requiring less sample volume, more suited for probing the magnetic nature of single SrO layers. In RIXS, change in energy and momentum of the scattered photons is directly related to the electronic excitations in the solid [139]. Information on magnetic excitations can be inferred since photon angular momentum can transfer to electron spin via spin-flip processes [140]. This method has been used to study spin and magnetic excitations in highly doped [141] and underdoped [142] cuprates as well as spin density waves in chromium [143].

7.2.3 Summary

In this section, we discussed potential future works to build off of and corroborate with previous experiments. By combining experimental achievement in heterostructure design, emergent phenomena, and device development, we propose a possible avenue for decoupling the many degrees of freedom in the quantum well heterostructures, and providing a possible avenue for the control of emergent magnetic features. In addition, we suggest a series of neutron reflectivity experiments to further confirm the presence of magnetic order in the thinnest quantum well heterostructures, thereby confirming what transport measurements have indicated, lending validity to the observation of emergent ferromagnetism in $GdTiO_3/SrTiO_3/GdTiO_3$. For magnetic order in $SmTiO_3/SrTiO_3/SmTiO_3$, we propose the use of resonant inelastic x-ray scattering to look for magnetic order in the thinnest $SrTiO_3$ quantum wells.

Bibliography

[1] J.-S. Zhou, J. Goodenough, and B. Dabrowski. Pressure-Induced Non-Fermi-Liquid Behavior of PrNiO3. *Physical Review Letters*, 94(22):3–6, June 2005.

[2] Clayton A. Jackson and Susanne Stemmer. Interface-induced magnetism in perovskite quantum wells. *Physical Review B*, 88(18):180403, November 2013.

[3] Jack Y. Zhang, Clayton A. Jackson, Santosh Raghavan, Jinwoo Hwang, and Susanne Stemmer. Magnetism and local structure in low-dimensional Mott insulating $GdTiO_3$. *Physical Review B*, 88(12):121104, September 2013.

[4] Jack Y. Zhang, Clayton A. Jackson, Ru Chen, Santosh Raghavan, Pouya Moetakef, Leon Balents, and Susanne Stemmer. Correlation between metal-insulator transitions and structural distortions in high-electron-density $SrTiO_3$ quantum wells. *Physical Review B*, 89(7):075140, February 2014.

[5] Pouya Moetakef, James R. Williams, Daniel G. Ouellette, Adam P. Kajdos, David Goldhaber-Gordon, S. James Allen, and Susanne Stemmer. Carrier-Controlled Ferromagnetism in $SrTiO_3$. *Physical Review X*, 2(2):021014, June 2012.

[6] H D Zhou and J B Goodenough. Localized or itinerant TiO_3 electrons in $RTiO_3$ perovskites. *Journal of Physics: Condensed Matter*, 17(46):7395–7406, November 2005.

[7] G Amow. Peculiar Magnetism of the $Sm_{(1-x)}Gd_xTiO_3$ System. *Journal of Solid State Chemistry*, 154(2):619–625, November 2000.

[8] Bharat Jalan, Roman Engel-Herbert, Joel Cagnon, and Susanne Stemmer. Growth modes in metal-organic molecular beam epitaxy of TiO_2 on r-plane sapphire. *Journal of Vacuum Science & Technology A: Vacuum, Surfaces, and Films*, 27(2):230, 2009.

[9] Julie A. Bert, Beena Kalisky, Christopher Bell, Minu Kim, Yasuyuki Hikita, Harold Y. Hwang, and Kathryn A. Moler. Direct imaging of the coexistence of ferromagnetism and superconductivity at the $LaAlO_3/SrTiO_3$ interface. *Nature Physics*, 7(10):767–771, September 2011.

[10] J Biscaras, N Bergeal, A Kushwaha, T Wolf, A Rastogi, R C Budhani, and J Lesueur. Two-dimensional superconductivity at a Mott insulator/band insulator interface $LaTiO_3/SrTiO_3$. *Nature communications*, 1:89, January 2010.

[11] Lu Li, C. Richter, J. Mannhart, and R. C. Ashoori. Coexistence of magnetic order and two-dimensional superconductivity at$LaAlO_3/SrTiO_3$ interfaces. *Nature Physics*, 7(10):762–766, September 2011.

[12] Satoshi Okamoto and Andrew Millis. Theory of Mott insulatorband insulator heterostructures. *Physical Review B*, 70(7):1–12, August 2004.

[13] Susanne Stemmer and Andrew J. Millis. Quantum confinement in oxide quantum wells. *MRS Bulletin*, 38(12):1032–1039, December 2013.

[14] Pavlo Zubko, Stefano Gariglio, Marc Gabay, Philippe Ghosez, and Jean-Marc Triscone. Interface Physics in Complex Oxide Heterostructures. *Annual Review of Condensed Matter Physics*, 2(1):141–165, March 2011.

[15] H Y Hwang, Y Iwasa, M Kawasaki, B Keimer, N Nagaosa, and Y Tokura. Emergent phenomena at oxide interfaces. *Nature materials*, 11(2):103–13, February 2012.

[16] Anand Bhattacharya and Steven J. May. Magnetic Oxide Heterostructures. *Annual Review of Materials Research*, 44(1):65–90, July 2014.

[17] P.A. Cox. *Transition Metal Oxides*. Clarendon Press, Oxford, 1992.

[18] K Jin, N P Butch, K Kirshenbaum, J Paglione, and R L Greene. Link between spin fluctuations and electron pairing in copper oxide superconductors. *Nature*, 476(7358):73–5, August 2011.

[19] T ru Moriya and Kazuo Ueda. Antiferromagnetic spin fluctuation and superconductivity. *Reports on Progress in Physics*, 66(8):1299–1341, August 2003.

[20] Piers Coleman and Andrew J Schofield. Quantum criticality. *Nature*, 433(7023):226–9, January 2005.

[21] Matthias Vojta. Quantum phase transitions. *Reports on Progress in Physics*, 66(12):2069–2110, December 2003.

[22] Marc De Graef McHenry and Michael E. *Structure of Materials*. Cambridge University Press, Cambridge.

[23] N. A. Pertsev, A. G. Zembilgotov, S. Hoffmann, R. Waser, and A. K. Tagantsev. Ferroelectric thin films grown on tensile substrates: Renormalization of the Curie-Weiss law and apparent absence of ferroelectricity. *Journal of Applied Physics*, 85(3):1698, February 1999.

[24] Na Sai, Craig Fennie, and Alexander Demkov. Absence of Critical Thickness in an Ultrathin Improper Ferroelectric Film. *Physical Review Letters*, 102(10):1–4, March 2009.

[25] S Gariglio, N Reyren, A D Caviglia, and J-M Triscone. Superconductivity at the $LaAlO_3$/$SrTiO_3$ interface. *Journal of physics. Condensed matter : an Institute of Physics journal*, 21(16):164213, April 2009.

[26] J. Hubbard. Electron Correlations in Narrow Energy Bands. *Proceedings of the Royal Society A: Mathematical, Physical and Engineering Sciences*, 276(1365):238–257, November 1963.

[27] N F Mott. The Basis of the Electron Theory of Metals, with Special Reference to the Transition Metals. *Proceedings of the Physical Society. Section A*, 62(7):416–422, July 1949.

[28] N. F. Mott. *Metal Insulator Transtions*, volume 70. Tylor and Francis, 1990.

[29] D. Dikin, M. Mehta, C. Bark, C. Folkman, C. Eom, and V. Chandrasekhar. Coexistence of Superconductivity and Ferromagnetism in Two Dimensions. *Physical Review Letters*, 107(5), July 2011.

[30] Masatoshi Imada, Atsushi Fujimori, and Yoshinori Tokura. Metal-insulator transitions. *Reviews of Modern Physics*, 70(4):1039–1263, October 1998.

[31] Shigeki Miyasaka, Hidenori Takagi, Yoshiaki Sekine, Hiroki Takahashi, Nobuo Môri, and Robert J. Cava. Metal-Insulator Transition and Itinerant Antiferromagnetism in $NiS_{2-x}Se_x$ Pyrite. *Journal of the Physics Society Japan*, 69(10):3166–3169, October 2000.

[32] J. Orenstein and A. Vishwanath. Doped Mott insulators: Breaking through to the other side. *Nature Physics*, 6(8):566–567, August 2010.

[33] G. Catalan, R. Bowman, and J. Gregg. Metal-insulator transitions in $NdNiO_3$ thin films. *Physical Review B*, 62(12):7892–7900, September 2000.

[34] I H Inoue. Electrostatic carrier doping to perovskite transition-metal oxides. *Semiconductor Science and Technology*, 20(4):S112–S120, April 2005.

[35] T. Katsufuji, Y. Okimoto, T. Arima, Y. Tokura, and J. Torrance. Optical spectroscopy of the metal-insulator transition in $NdNiO_3$. *Physical Review B*, 51(8):4830–4835, February 1995.

[36] SungBin Lee, Ru Chen, and Leon Balents. Landau Theory of Charge and Spin Ordering in the Nickelates. *Physical Review Letters*, 106(1), January 2011.

[37] Jun Akimitsu, Hirohiko Ichikawa, Naotoshi Eguchi, Tomoko Miyano, Masakazu Nishi, and Kazuhisa Kakurai. Direct Observation of Orbital Ordering in $YTiO_3$ by Means of the Polarized Neutron Diffraction Technique. *Journal of the Physical Society of Japan*, 70(12):3475–3478, December 2001.

[38] Masayuki Itoh, Michitoshi Tsuchiya, Hirotaka Tanaka, and Kiyoichiro Motoya. Orbital Ordering and Local Magnetic Properties of Mott-Hubbard Insulators $YTiO_3$ and $LaTiO_3$: NMR Study. *Journal of the Physical Society of Japan*, 68(8):2783–2789, August 1999.

[39] K. Takubo, M. Shimuta, J. E. Kim, K. Kato, M. Takata, and T. Katsufuji. Crossover behavior of the crystal structure and the relation to magnetism in perovskite $RTiO_3$. *Physical Review B*, 82(2):020401, July 2010.

[40] H. Nakao, Y. Wakabayashi, T. Kiyama, Y. Murakami, M. Zimmermann, J. Hill, Doon Gibbs, S. Ishihara, Y. Taguchi, and Y. Tokura. Quantitative determination of the atomic scattering tensor in orbitally ordered $YTiO_3$ by using a resonant x-ray scattering technique. *Physical Review B*, 66(18):184419, November 2002.

[41] Robert Schmitz, Ora Entin-Wohlman, Amnon Aharony, A. Harris, and Erwin Müller-Hartmann. Magnetic structure of the Jahn-Teller system $LaTiO_3$. *Physical Review B*, 71(14):144412, April 2005.

[42] E. Pavarini, S. Biermann, A. Poteryaev, A. Lichtenstein, A. Georges, and O. Andersen. Mott Transition and Suppression of Orbital Fluctuations in Orthorhombic 3d1 Perovskites. *Physical Review Letters*, 92(17):176403, April 2004.

[43] a. Komarek, H. Roth, M. Cwik, W.-D. Stein, J. Baier, M. Kriener, F. Bourée, T. Lorenz, and M. Braden. Magnetoelastic coupling in $RTiO_3$ (R=La,Nd,Sm,Gd,Y) investigated with diffraction techniques and thermal expansion measurements. *Physical Review B*, 75(22):1–12, June 2007.

[44] Takashi Kiyama and Masayuki Itoh. Presence of 3d Quadrupole Moment in $LaTiO_3$ Studied by NMR. *Physical Review Letters*, 91(16):167202, October 2003.

[45] Clayton A Jackson, Jack Y Zhang, Christopher R Freeze, and Susanne Stemmer. Quantum critical behaviour in confined $SrTiO_3$ quantum wells embedded in antiferromagnetic $SmTiO_3$. *Nature communications*, 5:4258, January 2014.

[46] G. Conti, A. M. Kaiser, A. X. Gray, S. Nemsak, G. K. Palsson, J. Son, P. Moetakef, A. Janotti, L. Bjaalie, C. S. Conlon, D. Eiteneer, A. A. Greer, A. Keqi, A. Rattanachata, A. Y. Saw, A. Bostwick, W. C. Stolte, A. Gloskovskii, W. Drube, S. Ueda, M. Kobata, K. Kobayashi, C. G. Van de Walle, S. Stemmer, C. M. Schneider, and C. S. Fadley. Band offsets in complex-oxide thin films and heterostructures of $SrTiO_3$/$LaNiO_3$ and $SrTiO_3$/$GdTiO_3$ by soft and hard X-ray photoelectron spectroscopy. *Journal of Applied Physics*, 113(14):143704, April 2013.

[47] Brian M. McSkimming, F. Wu, Thomas Huault, Catherine Chaix, and James S. Speck. Plasma assisted molecular beam epitaxy of GaN with growth rates >2.6 μm/h. *Journal of Crystal Growth*, 386:168–174, January 2014.

[48] P. B. Joyce, T. J. Krzyzewski, G. R. Bell, and T. S. Jones. Effect of growth rate on the size, composition, and optical properties of InAs/GaAs quantum dots grown by molecular-beam epitaxy. *Physical Review B*, 62(16):10891–10895, October 2000.

[49] Bharat Jalan, Roman Engel-Herbert, Nicholas J. Wright, and Susanne Stemmer. Growth of high-quality $SrTiO_3$ films using a hybrid molecular beam epitaxy approach. *Journal of Vacuum Science & Technology A: Vacuum, Surfaces, and Films*, 27(3):461, 2009.

[50] Marian A. Herman, W. Richter, and Helmut Sitter. *Epitaxy: Physical Principles and Technical Implementation*. Springer, 2004.

[51] R.A. Swalin. *Thermodynamics of solids*. John Wiley & Sons, New York, 1972.

[52] Bharat Jalan, Joel Cagnon, Thomas E. Mates, and Susanne Stemmer. Analysis of carbon in $SrTiO_3$ grown by hybrid molecular beam epitaxy. *Journal of Vacuum Science & Technology A: Vacuum, Surfaces, and Films*, 27(6):1365, 2009.

[53] Tyler A. Cain, Adam P. Kajdos, and Susanne Stemmer. La-doped $SrTiO_3$ films with large cryogenic thermoelectric power factors. *Applied Physics Letters*, 102(18):182101, May 2013.

[54] B. E. Warren. *X-ray Diffraction*. Dover Publications, inc, New York, 1990.

[55] Amit Verma, Adam P. Kajdos, Tyler A. Cain, Susanne Stemmer, and Debdeep Jena. Intrinsic Mobility Limiting Mechanisms in Lanthanum-Doped Strontium Titanate. *Physical Review Letters*, 112(21):216601, May 2014.

[56] Pouya Moetakef, Daniel G. Ouellette, Jack Y. Zhang, Tyler A. Cain, S. James Allen, and Susanne Stemmer. Growth and properties of $GdTiO_3$ films prepared by hybrid molecular beam epitaxy. *Journal of Crystal Growth*, 355(1):166–170, 2012.

[57] A method of measuring the resistivity and Hall coefficient of lamellae of arbitrary shape. *Philips Tech. Rev.*, 20:220–224, 1958.

[58] Jun Kondo. Anomalous Hall Effect and Magnetoresistance of Ferromagnetic Metals. *Progress of Theoretical Physics*, 27(4):772–792, April 1962.

[59] H. Nakayama, M. Althammer, Y.-T. Chen, K. Uchida, Y. Kajiwara, D. Kikuchi, T. Ohtani, S. Geprägs, M. Opel, S. Takahashi, R. Gross, G. E. W. Bauer, S. T. B. Goennenwein, and E. Saitoh. Spin Hall Magnetoresistance Induced by a Nonequilibrium Proximity Effect. *Physical Review Letters*, 110(20):206601, May 2013.

[60] N. Vlietstra, J. Shan, V. Castel, J. Ben Youssef, G. E. W. Bauer, and B. J. van Wees. Exchange magnetic field torques in YIG/Pt bilayers observed by the spin-Hall magnetoresistance. page 4, May 2013.

[61] C. Hahn, G. de Loubens, O. Klein, M. Viret, V. V. Naletov, and J. Ben Youssef. Comparative measurements of inverse spin Hall effects and magnetoresistance in YIG/Pt and YIG/Ta. *Physical Review B*, 87(17):174417, May 2013.

[62] H. J. Schulz. Fermi liquids and non–Fermi liquids. March 1995.

[63] A. J. Schofield. Non-Fermi liquids. *Contemporary Physics*, 40(2):95–115, March 1999.

[64] W. G. Baber. The Contribution to the Electrical Resistance of Metals from Collisions between Electrons. *Proceedings of the Royal Society A: Mathematical, Physical and Engineering Sciences*, 158(894):383–396, January 1937.

[65] Hilbert v Löhneysen. Fermi-liquid instability at magneticnonmagnetic quantum phase transitions. *Journal of Magnetism and Magnetic Materials*, 200(1-3):532–551, October 1999.

[66] James M. Rondinelli, Steven J. May, and John W. Freeland. Control of octahedral connectivity in perovskite oxide heterostructures: An emerging route to multifunctional materials discovery. *MRS Bulletin*, 37(03):261–270, March 2012.

[67] Jinwoo Hwang, Jack Zhang, Adrian DAlfonso, Leslie Allen, and Susanne Stemmer. Three-Dimensional Imaging of Individual Dopant Atoms in $SrTiO_3$. *Physical Review Letters*, 111(26):266101, December 2013.

[68] A. M. Glazer. The classification of tilted octahedra in perovskites. *Acta Crystallographica Section B Structural Crystallography and Crystal Chemistry*, 28(11):3384–3392, November 1972.

[69] P. M. Woodward. Octahedral Tilting in Perovskites. II. Structure Stabilizing Forces. *Acta Crystallographica Section B Structural Science*, 53(1):44–66, February 1997.

[70] Masahito Mochizuki and Masatoshi Imada. Orbital physics in the perovskite Ti oxides. *New Journal of Physics*, 6(1):154–154, November 2004.

[71] John B. Goodenough and J.-S. Zhou. Orbital ordering in orthorhombic perovskites. *Journal of Materials Chemistry*, 17(23):2394, June 2007.

[72] M. Kubota, H. Nakao, Y. Murakami, Y. Taguchi, M. Iwama, and Y. Tokura. Orbital ordering near a Mott transition:Resonant x-ray scattering study of the perovskite Ti oxides RTiO3 and $LaTiO_3$.02 (R=Gd, Sm, Nd, and La). *Physical Review B*, 70(24):1–8, December 2004.

[73] E Pavarini, A Yamasaki, J Nuss, and O K Andersen. How chemistry controls electron localization in $3d^1$ perovskites: a Wannier-function study. *New Journal of Physics*, 7(1):188–188, September 2005.

[74] Jack Y. Zhang, Jinwoo Hwang, Santosh Raghavan, and Susanne Stemmer. Symmetry Lowering in Extreme-Electron-Density Perovskite Quantum Wells. *Physical Review Letters*, 110(25):256401, June 2013.

[75] Carl W. Turner and J.E. Greedan. Ferrimagnetism in the rare earth titanium (III) oxides, $RTiO_3$; R = Gd, Tb, Dy, Ho, Er, Tm. *Journal of Solid State Chemistry*, 34(2):207–213, September 1980.

[76] Pouya Moetakef, Jack Y. Zhang, Santosh Raghavan, Adam P. Kajdos, and Susanne Stemmer. Growth window and effect of substrate symmetry in hybrid

molecular beam epitaxy of a Mott insulating rare earth titanate. *Journal of Vacuum Science & Technology A: Vacuum, Surfaces, and Films*, 31(4):041503, May 2013.

[77] Laura Roth. Simple Narrow-Band Model of Ferromagnetism Due to Intra-Atomic Exchange. *Physical Review*, 149(1):306–308, September 1966.

[78] Satoru Inagaki. Effect of Orbital Degeneracy and Intra-Atomic Exchange on the Occurrence of Ferromagnetism. *Journal of the Physical Society of Japan*, 39(3):596–604, March 1975.

[79] D.I. Khomskii and K.I. Kugel. Orbital and magnetic structure of two-dimensional ferromagnets with Jahn-Teller ions. *Solid State Communications*, 13(7):763–766, October 1973.

[80] Pouya Moetakef, Clayton A. Jackson, Jinwoo Hwang, Leon Balents, S. James Allen, and Susanne Stemmer. Toward an artificial Mott insulator: Correlations in confined high-density electron liquids in $SrTiO_3$. *Physical Review B*, 86(20):201102, November 2012.

[81] Pouya Moetakef, Tyler A. Cain, Daniel G. Ouellette, Jack Y. Zhang, Dmitri O. Klenov, Anderson Janotti, Chris G. Van de Walle, Siddharth Rajan, S. James Allen, and Susanne Stemmer. Electrostatic carrier doping of $GdTiO_3$/$SrTiO_3$ interfaces. *Applied Physics Letters*, 99(23):232116, December 2011.

[82] K. Yoshimatsu, T. Okabe, H. Kumigashira, S. Okamoto, S. Aizaki, A. Fujimori, and M. Oshima. Dimensional-Crossover-Driven Metal-Insulator Transition in $SrVO_3$ Ultrathin Films. *Physical Review Letters*, 104(14):147601, April 2010.

[83] Junwoo Son, Pouya Moetakef, James M. LeBeau, Daniel Ouellette, Leon Balents, S. James Allen, and Susanne Stemmer. Low-dimensional Mott material: Transport in ultrathin epitaxial LaNiO[sub 3] films. *Applied Physics Letters*, 96(6):062114, 2010.

[84] Raoul Scherwitzl, Pavlo Zubko, I Gutierrez Lezama, Shimpei Ono, Alberto F Morpurgo, Gustau Catalan, and Jean-Marc Triscone. Electric-field control of the metal-insulator transition in ultrathin $NdNiO_3$ films. *Advanced materials (Deerfield Beach, Fla.)*, 22(48):5517–20, December 2010.

[85] A V Boris, Y Matiks, E Benckiser, A Frano, P Popovich, V Hinkov, P Wochner, M Castro-Colin, E Detemple, V K Malik, C Bernhard, T Prokscha, A Suter,

Z Salman, E Morenzoni, G Cristiani, H-U Habermeier, and B Keimer. Dimensionality control of electronic phase transitions in nickel-oxide superlattices. *Science (New York, N.Y.)*, 332(6032):937–40, May 2011.

[86] Jian Liu, M. Kareev, D. Meyers, B. Gray, P. Ryan, J. W. Freeland, and J. Chakhalian. Metal-Insulator Transition and Orbital Reconstruction in Mott-Type Quantum Wells Made of $NdNiO_3$. *Physical Review Letters*, 109(10):107402, September 2012.

[87] Feizhou He, B. Wells, Z.-G. Ban, S. Alpay, S. Grenier, S. Shapiro, Weidong Si, A. Clark, and X. Xi. Structural phase transition in epitaxial perovskite films. *Physical Review B*, 70(23):235405, December 2004.

[88] S. J. May, J.-W. Kim, J. M. Rondinelli, E. Karapetrova, N. A. Spaldin, A. Bhattacharya, and P. J. Ryan. Quantifying octahedral rotations in strained perovskite oxide films. *Physical Review B*, 82(1):014110, July 2010.

[89] Yan-Ting Chen, Saburo Takahashi, Hiroyasu Nakayama, Matthias Althammer, Sebastian T. B. Goennenwein, Eiji Saitoh, and Gerrit E. W. Bauer. Theory of spin Hall magnetoresistance. *Physical Review B*, 87(14):144411, April 2013.

[90] Hung T. Dang and Andrew J. Millis. Designing ferromagnetism in vanadium oxide based superlattices. *Physical Review B*, 87(18):184434, May 2013.

[91] Daniel G Ouellette, Pouya Moetakef, Tyler A Cain, Jack Y Zhang, Susanne Stemmer, David Emin, and S James Allen. High-density two-dimensional small polaron gas in a delta-doped Mott insulator. *Scientific reports*, 3:3284, January 2013.

[92] Jay D. Sau, Roman M. Lutchyn, Sumanta Tewari, and S. Das Sarma. Generic New Platform for Topological Quantum Computation Using Semiconductor Heterostructures. *Physical Review Letters*, 104(4):040502, January 2010.

[93] Arne Brataas, Andrew D Kent, and Hideo Ohno. Current-induced torques in magnetic materials. *Nature materials*, 11(5):372–81, May 2012.

[94] Jason Alicea. New directions in the pursuit of Majorana fermions in solid state systems. *Reports on progress in physics. Physical Society (Great Britain)*, 75(7):076501, July 2012.

[95] Zhicheng Zhong, Anna Tóth, and Karsten Held. Theory of spin-orbit coupling at $LaAlO_3/SrTiO_3$ interfaces and $SrTiO_3$ surfaces. *Physical Review B*, 87(16):161102, April 2013.

[96] Younghyun Kim, Roman M. Lutchyn, and Chetan Nayak. Origin and Transport Signatures of Spin-Orbit Interactions in One- and Two-Dimensional $SrTiO_3$-Based Heterostructures. April 2013.

[97] Lorien H. Hayden, R. Raimondi, M. E. Flatte', and G. Vignale. Intrinsic Spin Hall Effect at Oxide Interfaces: a Simple Model. page 22, April 2013.

[98] a. D. Caviglia, M. Gabay, S. Gariglio, N. Reyren, C. Cancellieri, and J.-M. Triscone. Tunable Rashba Spin-Orbit Interaction at Oxide Interfaces. *Physical Review Letters*, 104(12):126803, March 2010.

[99] F Iga, T Naka, T Matsumoto, N Shirakawa, K Murata, and Y Nishihara. Study of first-order metal-insulator transition in the strongly correlated electron system $Y_{1-x}Ca_xTiO_3$. *Physica B: Condensed Matter*, 223-224:526–528, June 1996.

[100] Xiaopeng Li, W. Vincent Liu, and Leon Balents. Spirals and Skyrmions in Two Dimensional Oxide Heterostructures. *Physical Review Letters*, 112(6):067202, February 2014.

[101] Guru Khalsa, Byounghak Lee, and A. H. MacDonald. *Phys. Rev. B*.

[102] Pouya Moetakef, Daniel G. Ouellette, James R. Williams, S. James Allen, Leon Balents, David Goldhaber-Gordon, and Susanne Stemmer. Quantum oscillations from a two-dimensional electron gas at a Mott/band insulator interface. *Applied Physics Letters*, 101(15):151604, October 2012.

[103] Tyler A. Cain, SungBin Lee, Pouya Moetakef, Leon Balents, Susanne Stemmer, and S. James Allen. Seebeck coefficient of a quantum confined, high-electron-density electron gas in $SrTiO_3$. *Applied Physics Letters*, 100(16):161601, April 2012.

[104] Ion Garate, Jairo Sinova, T. Jungwirth, and A. MacDonald. Theory of weak localization in ferromagnetic (Ga,Mn)As. *Physical Review B*, 79(15):155207, April 2009.

[105] V. Dugaev, P. Bruno, and J. Barnaś. Weak localization in ferromagnets with spin-orbit interaction. *Physical Review B*, 64(14):144423, September 2001.

[106] T. McGuire and R. Potter. Anisotropic magnetoresistance in ferromagnetic 3d alloys. *IEEE Transactions on Magnetics*, 11(4):1018–1038, July 1975.

[107] T. Jungwirth, M. Abolfath, Jairo Sinova, J. Kucera, and A. H. MacDonald. Boltzmann theory of engineered anisotropic magnetoresistance in (Ga,Mn)As. *Applied Physics Letters*, 81(21):4029, November 2002.

[108] Tôru Moriya, Yoshinori Takahashi, and Kazuo Ueda. Antiferromagnetic Spin Fluctuations and Superconductivity in Two-Dimensional Metals -A Possible Model for High T_c Oxides. *Journal of the Physics Society Japan*, 59(8):2905–2915, August 1990.

[109] G. Stewart. Non-Fermi-liquid behavior in d- and f-electron metals. *Reviews of Modern Physics*, 73(4):797–855, October 2001.

[110] Hilbert v. Löhneysen and Peter Wölfle. Fermi-liquid instabilities at magnetic quantum phase transitions. *Reviews of Modern Physics*, 79(3):1015–1075, August 2007.

[111] A. Rosch. Interplay of Disorder and Spin Fluctuations in the Resistivity near a Quantum Critical Point. *Physical Review Letters*, 82(21):4280–4283, May 1999.

[112] E Miranda and V Dobrosavljević. Disorder-driven non-Fermi liquid behaviour of correlated electrons. *Reports on Progress in Physics*, 68(10):2337–2408, October 2005.

[113] T. Kirkpatrick and D. Belitz. Quantum critical behavior of disordered itinerant ferromagnets. *Physical Review B*, 53(21):14364–14376, June 1996.

[114] H D Zhou and J B Goodenough. Localized or itinerant TiO_3 electrons in $RTiO_3$ perovskites. *Journal of Physics: Condensed Matter*, 17(46):7395–7406, November 2005.

[115] Ru Chen, SungBin Lee, and Leon Balents. Dimer Mott insulator in an oxide heterostructure. *Physical Review B*, 87(16):161119, April 2013.

[116] S E Sebastian, N Harrison, C D Batista, L Balicas, M Jaime, P A Sharma, N Kawashima, and I R Fisher. Dimensional reduction at a quantum critical point. *Nature*, 441(7093):617–20, June 2006.

[117] Hiroshi Yamada and Satoshi Takada. Magnetoresistance of Antiferromagnetic Metals Due to s-d Interaction. *Journal of the Physical Society of Japan*, 34(1):51–57, January 1973.

[118] S. Klimm, G. Gerstmeier, H. Paulin, M. Klemm, and S. Horn. Magnetic anisotropy in the SDW state of metallic V_2O_3 observed by magnetotransport measurements on oriented single crystals. *Physica B: Condensed Matter*, 230-232:992–995, February 1997.

[119] N. E. Sluchanko, A. N. Azarevich, A. V. Bogach, V. V. Glushkov, S. V. Demishev, A. V. Levchenko, V. B. Filippov, and N. Yu. Shitsevalova. Specific features of magnetoresistance during the antiferromagnet-paramagnet transition in $Tm_{1-x}Yb_x\ B_{12}$. *Journal of Experimental and Theoretical Physics*, 116(5):866–871, June 2013.

[120] J. Dong, H. J. Zhang, G. Xu, Z. Li, G. Li, W. Z. Hu, D. Wu, G. F. Chen, X. Dai, J. L. Luo, Z. Fang, and N. L. Wang. Competing orders and spin-density-wave instability in $La_{(1-x)}F_x$FeAs. *EPL (Europhysics Letters)*, 83(2):27006, July 2008.

[121] Santosh Raghavan, S. James Allen, and Susanne Stemmer. Subband structure of two-dimensional electron gases in $SrTiO_3$. *Applied Physics Letters*, 103(21):212103, November 2013.

[122] Gerd Bergmann. Weak localization in thin films. *Physics Reports*, 107(1):1–58, May 1984.

[123] J. H. Ngai, Y. Segal, D. Su, Y. Zhu, F. J. Walker, S. Ismail-Beigi, K. Le Hur, and C. H. Ahn. Electric field tuned crossover from classical to weakly localized quantum transport in electron doped $SrTiO_3$. *Physical Review B*, 81(24):241307, June 2010.

[124] T. Hernandez, C. W. Bark, D. A. Felker, C. B. Eom, and M. S. Rzchowski. Localization of two-dimensional electron gas in $LaAlO_3$/$SrTiO_3$ heterostructures. *Physical Review B*, 85(16):161407, April 2012.

[125] Franklin J. Wong, Seung-Hyub Baek, Rajesh V. Chopdekar, Virat V. Mehta, Ho-Won Jang, Chang-Beom Eom, and Yuri Suzuki. Metallicity in $LaTiO_3$ thin films induced by lattice deformation. *Physical Review B*, 81(16):2–5, April 2010.

[126] U.K. Mishra and P. Parikh. AlGaN/GaN HEMTs-an overview of device operation and applications. *Proceedings of the IEEE*, 90(6):1022–1031, June 2002.

[127] a Ohtomo, D a Muller, J L Grazul, and H Y Hwang. Artificial charge-modulation in atomic-scale perovskite titanate superlattices. *Nature*, 419(6905):378–80, September 2002.

[128] J. Kim, S. Seo, M. Chisholm, R. Kremer, H.-U. Habermeier, B. Keimer, and H. Lee. Nonlinear Hall effect and multichannel conduction in $LaTiO_3$/$SrTiO_3$ superlattices. *Physical Review B*, 82(20):2–5, November 2010.

[129] C. H. Ahn, M. Di Ventra, J. N. Eckstein, C. Daniel Frisbie, M. E. Gershenson, A. M. Goldman, I. H. Inoue, J. Mannhart, Andrew J. Millis, Alberto F. Morpurgo, Douglas Natelson, and Jean-Marc Triscone. Electrostatic modification of novel materials. *Reviews of Modern Physics*, 78(4):1185–1212, November 2006.

[130] J.D. Wiley. C-V profiling of GaAs FET films. *IEEE Transactions on Electron Devices*, 25(11):1317–1324, November 1978.

[131] J.D. Wiley. Series resistance Effects in Semiconductor CV profiling. *Electron Devices, IEEE Transactions on*, (5):265–272, 1975.

[132] Pouya Moetakef, Jack Y. Zhang, Alexander Kozhanov, Bharat Jalan, Ram Seshadri, S. James Allen, and Susanne Stemmer. Transport in ferromagnetic $GdTiO_3/SrTiO_3$ heterostructures. *Applied Physics Letters*, 98(11):112110, 2011.

[133] R. C. Neville. Permittivity of Strontium Titanate. *Journal of Applied Physics*, 43(5):2124, May 1972.

[134] T. Sakudo and H. Unoki. Dielectric Properties of $SrTiO_3$ at Low Temperatures. *Physical Review Letters*, 26(14):851–853, April 1971.

[135] A.K. Tagantsev, V.O. Sherman, K.F. Astafiev, J. Venkatesh, and N. Setter. Ferroelectric Materials for Microwave Tunable Applications. *Journal of Electroceramics*, 11(1/2):5–66, September 2003.

[136] R. C. Neville and B. Hoeneisen. Anomalous capacitance of Schottky barriers on strontium titanate. *Journal of Applied Physics*, 46(1):350, September 1975.

[137] M. Boucherit, O. F. Shoron, T. A. Cain, C. A. Jackson, S. Stemmer, and S. Rajan. Extreme charge density $SrTiO_3/GdTiO_3$ heterostructure field effect transistors. *Applied Physics Letters*, 102(24):242909, June 2013.

[138] M. Boucherit, O. Shoron, C. A. Jackson, T. A. Cain, M. L. C. Buffon, C. Polchinski, S. Stemmer, and S. Rajan. Modulation of over 10^{14} $\mathrm{cm}-2$ electrons in $SrTiO_3/GdTiO_3$ heterostructures. *Applied Physics Letters*, 104(18):182904, May 2014.

[139] Akio Kotani and Shik Shin. Resonant inelastic x-ray scattering spectra for electrons in solids. *Reviews of Modern Physics*, 73(1):203–246, February 2001.

[140] Luuk Ament, Giacomo Ghiringhelli, Marco Sala, Lucio Braicovich, and Jeroen van den Brink. Theoretical Demonstration of How the Dispersion of Magnetic Excitations in Cuprate Compounds can be Determined Using Resonant Inelastic X-Ray Scattering. *Physical Review Letters*, 103(11):117003, September 2009.

[141] M. Le Tacon, M. Minola, D. C. Peets, M. Moretti Sala, S. Blanco-Canosa, V. Hinkov, R. Liang, D. A. Bonn, W. N. Hardy, C. T. Lin, T. Schmitt, L. Braicovich, G. Ghiringhelli, and B. Keimer. Dispersive spin excitations in highly overdoped cuprates revealed by resonant inelastic x-ray scattering. *Physical Review B*, 88(2):020501, July 2013.

[142] L. Braicovich, J. van den Brink, V. Bisogni, M. Moretti Sala, L. J. P. Ament, N. B. Brookes, G. M. De Luca, M. Salluzzo, T. Schmitt, V. N. Strocov, and G. Ghiringhelli. Magnetic Excitations and Phase Separation in the Underdoped $La_{2-x}Sr_xCuO_4$ Superconductor Measured by Resonant Inelastic X-Ray Scattering. *Physical Review Letters*, 104(7):077002, February 2010.

[143] Koudai Sugimoto, Zhi Li, Eiji Kaneshita, Kenji Tsutsui, and Takami Tohyama. Spin dynamics and resonant inelastic x-ray scattering in chromium with commensurate spin-density wave order. *Physical Review B*, 87(13):134418, April 2013.

[144] Bharat Jalan, Roman Engel-Herbert, Nicholas J. Wright, and Susanne Stemmer. Growth of high-quality $SrTiO_3$ films using a hybrid molecular beam epitaxy approach. *Journal of Vacuum Science & Technology A: Vacuum, Surfaces, and Films*, 27(3):461, March 2009.

[145] Bharat Jalan, Pouya Moetakef, and Susanne Stemmer. Molecular beam epitaxy of $SrTiO_3$ with a growth window. *Applied Physics Letters*, 95(3):032906, July 2009.

Appendix A

Growth of $SmTiO_3$

Here, we briefly discuss the details of the development of a $SmTiO_3$ growth window. The basic method is similar to the growth method employed for both $SrTiO_3$ and $GdTiO_3$ described in more detail in references [52, 144, 145, 56, 76].

As discussed in Chapter 2, a hybrid MBE technique is employed for the growth of $SmTiO_3$. Because of the instability of Ti^{3+} in the presence of oxygen, stabilization of the perovskite phase can be challenging, and a pyrochlore phase [56] is often found. Thus, the growth must be accommodated at very low oxygen pressures, accomplished by only relying on the TTIP for oxygen. Furthermore, to avoid the accumulation of oxygen in the chamber during growth, the flux rates are turned down as low as possible, the limiting factor only being precision control of the TTIP pressure with a linear leak valve.

All films were grown on insulating (001) LSAT substrates. The substrates were backed with 350 nm of Ta to improve thermal coupling to the substrate heater. The growth temperature was kept at 900°C, based on the growth of $GdTiO_3$ and $SrTiO_3$. Prior to growth, the substrates were cleaned in acetone and isopropanol and baked at 200°C in the MBE load lock chamber.

To find a starting point for the growth of stoichiometric $SmTiO_3$, the deposition rates of TiO_2 and Sm_2O_3 were first estimated for growth at different cell temperatures for Sm and pressures for TTIP. This was accomplished by deposition of TTIP and Sm on LSAT, respectively. The films were allowed to oxidize in air and the thickness was measured with Dektak. These rates were then calibrated such that the two layers had the same shutter times, providing a starting point for codeposition growth.

Once a starting growth point was established, the ratio of TTIP to Sm flux was adjusted (calculated based on beam equivalent pressures), and a growth window was characterized using RHEED, x-ray diffraction, scanning transmission electron microscopy and transport properties.

Figure A.1 shows RHEED patterns for TTIP/Sm ratios ranging from 55 to 40. Within this ratio, RHEED images show smooth streaky patterns, indicative of a two-dimensional surface. Furthermore, intensity vs time for the specular streak (Figure A.2) reveal RHEED oscillations, indicative of a layer-by-layer growth mode [50]. From the RHEED oscillations, a growth rate of $\sim$ 20 nm/hr is estimated.

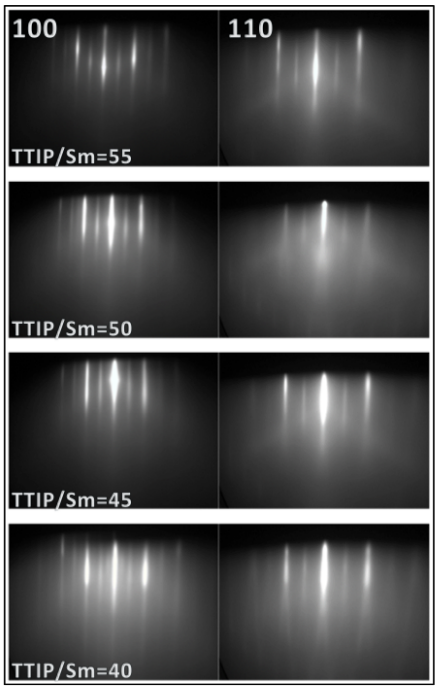

Figure A.1: RHEED images for the (100) and (110) crystal orientations and TTIP/Sm ratios ranging from 55 to 40.

X-ray diffraction patterns for TTIP/Sm ranging from 55 to 40 are featured in Figure A.3. Diffraction patterns show thickness fringes within this range and an out-of-plane lattice constant of $\sim$ 0.393 nm, in good agreement with strained, (110) oriented $SmTiO_3$ on (001) LSAT ($\sim$ 0.394 nm). The thickness fringes give a total film thickness in good agreement with film thicknesses estimated from RHEED oscillations, confirming a growth rate of $\sim$ 20 nm/hr. Within the growth window, STEM images (see Figure 5.2) show epitaxial, perovskite phase $SmTiO_3$.

Two-terminal electrical resistance measurements are featured in Figure 5.3. The results show an insulating film with a room temperature conductivity of 12.6 $(\Omega\ \mathrm{cm})^{-1}$ and an activation energy of 0.11 eV. Bulk polycrystalline data for $SmTiO_3$ gives a room

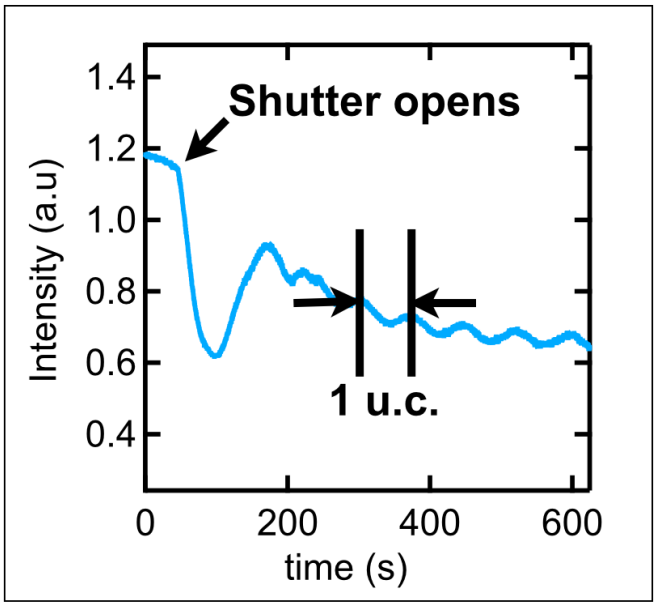

Figure A.2: RHEED intensity vs. time for the specular streak in the (100) orientation. The intensity shows oscillations, indicative of a layer-by-layer growth mode.

temperature conductivity of 0.24 $(\Omega\ \text{cm})^{-1}$ and an activation energy of 0.15 eV. The lesser activation energy could be a result of compressive strain leading to a narrowing of the Mott band gap [56]. Seebeck measurements show a p-type material and give a room temperature coefficient of $\sim$ 48 μV/K. Bulk polycrystalline $SmTiO_3$ gives a Seebeck of $\sim$ 110 μV/K.

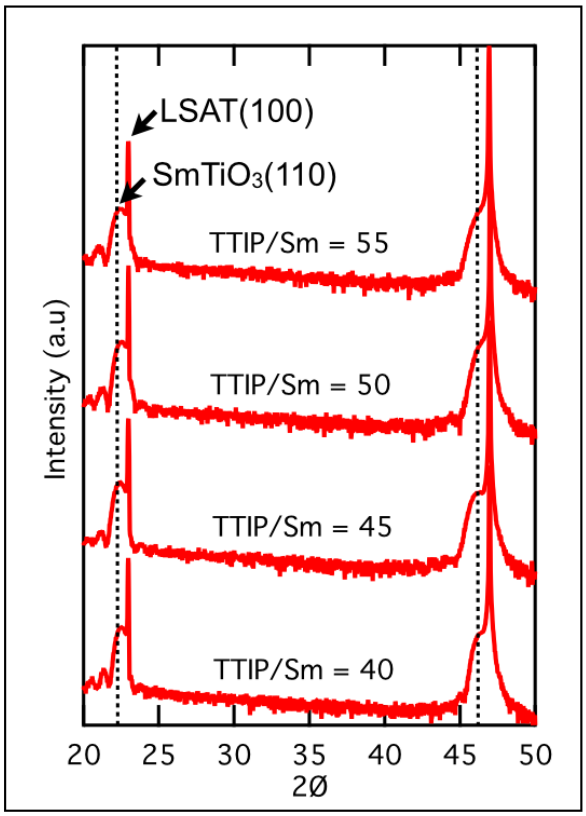

Figure A.3: High resolution x-ray diffraction patterns for 20 nm thick $SmTiO_3$ films grown on LSAT with TTIP/Sm ratios ranging from 55 to 40. All patterns within this growth window show thickness fringes and an out-of-plane lattice constant in close agreement with whats expected for strained (110) oriented $SmTiO_3$. The dashed lines are a guide to the eye.